

AD-A225 893

Semi-Annual Report

**Pseudomorphic Semiconducting Heterostructures from
Combinations of AlN, GaN and Selected SiC Polytypes: Theoretical
Advancement and its Coordination with Experimental Studies of
Nucleation, Growth, Characterization and Device Development**

DTIC
SELECTE
AUG 28 1990
S
D
D

Supported under Grant #N00014-90-J-1427
Department of the Navy
Office of the Chief of Naval Research
Report for the period January 1, 1990-June 30, 1990

Robert F. Davis, Max W. H. Braun, Larry Rowland and Zlatko Sitar
Materials Science and Engineering Department
North Carolina State University
Campus Box 7907
Raleigh, NC 27695-7907

DISTRIBUTION STATEMENT A
Approved for public release
Distribution Unlimited

July, 1990

REPORT DOCUMENTATION PAGE

Form Approved
OMB No. 0704-0188

Public reporting burden for this collection of information is estimated to average 1 hour per response, including the time for reviewing instructions, searching existing data sources, gathering and maintaining the data needed, and completing and reviewing the collection of information. Send comments regarding this burden estimate or any other aspect of this collection of information, including suggestions for reducing this burden to Washington Headquarters Services, Directorate for Information Operations and Reports, 1215 Jefferson Davis Highway, Suite 1204 Arlington, VA 22202-4302, and to the Office of Management and Budget, Paperwork Reduction Project (0704-0188) Arlington, VA 22203-3002

1. AGENCY USE ONLY (Leave blank)	2. REPORT DATE July, 1990	3. REPORT TYPE AND DATES COVERED Annual 1/1/90-6/30/90	
4. TITLE AND SUBTITLE Pseudomorphic Semiconducting Hetero-structures from Combinations of AlN, GaN and Selected SiC Polytypes: Theoretical Advancement and its Coordination with Experimental Studies		5. FUNDING NUMBERS 414s007---01 1114SS N00179 N66005 4B855	
6. AUTHOR(S) Robert F. Davis			
7. PERFORMING ORGANIZATION NAME(S) AND ADDRESS(ES) North Carolina State University Hillsborough Street Raleigh, NC 27695		8. PERFORMING ORGANIZATION REPORT NUMBER N00014-90-J-1427	
9. SPONSORING/MONITORING AGENCY NAME(S) AND ADDRESS(ES) Department of the Navy Office of the Chief of Naval Research 800 North Quincy, Code 1513:CMB Arlington, VA 22217-5000		10. SPONSORING/MONITORING AGENCY REPORT NUMBER	
11. SUPPLEMENTARY NOTES			
12a. DISTRIBUTION/AVAILABILITY STATEMENT Approved for Public Release; Distribution Unlimited		12b. DISTRIBUTION CODE	
13. ABSTRACT (Maximum 200 words) <div style="margin-left: 40px;"> <p>In this reporting period, studies have been conducted in three primary areas:</p> <p>(1) development and application of computer codes concerned with pseudomorphic structures (specifically the cBN-diamond system), the growth of GaN/AlN pseudomorphic heterostructures and the design and fabrication of a growth system for the deposition of SiC/AlN/GaN pseudomorphic structures. Low index planes [(111), (110), (100) and (221)] have been shown to be geometrically favorable for the growth of cBN on diamond. For the first time, pseudomorphic heterostructures between GaN and AlN have been achieved and characterized. An MBE/ALE system has been designed and is under construction for the deposition of AlN/GaN/SiC pseudomorphic heterostructures.</p> <p style="text-align: right;">— R H #</p> </div>			
14. SUBJECT TERMS pseudomorphic heterostructures, cubic boron nitride, diamond gallium nitride, aluminum nitride, molecular beam epitaxy, atomic layer epitaxy		15. NUMBER OF PAGES 51	
		16. PRICE CODE	
17. SECURITY CLASSIFICATION OF REPORT UNCLAS	18. SECURITY CLASSIFICATION OF THIS PAGE UNCLAS	19. SECURITY CLASSIFICATION OF ABSTRACT UNCLAS	20. LIMITATION OF ABSTRACT SAR

Table of Contents

I.	Introduction	1
II.	The Role of Geometric Considerations in the Diamond-Cubic Boron Nitride Heteroepitaxial System	2
	A. Introduction	2
	B. The Epitaxial Criterion	3
	C. Special Considerations in Covalent Polyatomic Systems	8
	D. Application to the Diamond - BN _{cub} System	8
	E. Conclusions	19
III.	AlN/GaN Multilayer and Pseudomorphic Heterostructures	20
	A. Introduction	20
	B. Growth Procedure	20
	C. Chemical Analysis	22
	D. Structural and Microstructural Analyses	24
	X-ray Rocking Curves	24
	Transmission Electron Microscopy	29
	E. Optical Characterization	32
IV.	Design and Construction of a Gas-Source MBE/ALE System for the Deposition of AlN/GaN/SiC Pseudomorphic Heterostructures	39
	A. Introduction	39
	B. Growth System and Concepts of Gas Flow Control	40
	C. Discussion	43
	D. Conclusions	46
V.	References	46

Accession For		↓
NTIS CRA&I		<input checked="" type="checkbox"/>
DTIC TAB		<input type="checkbox"/>
Unannounced		<input type="checkbox"/>
Justification		
By		
Distribution /		
Availability Codes		
Dist	Avail and/or Special	
A-1		



I. Introduction

The advent of techniques for growing semiconductor multilayer structures with layer thicknesses approaching atomic dimensions has provided new systems for both basic physics studies and device applications. Most of the research involving these structures has been restricted to materials with lattice constants that are equal within $\pm 0.1\%$. However it is now recognized that interesting and useful pseudomorphic structures can also be grown from a much larger set of materials that have lattice-constant mismatches in the percent range. Moreover, advances in computer hardware and software as well as the development of theoretical structural and molecular models applicable for strained layer nucleation, growth and property prediction have occurred to the extent that the field is poised to expand rapidly. It is in this context that the research described in this report is being conducted. The materials systems of concern include combinations of the direct bandgap materials of AlN and GaN and selected, indirect bandgap SiC polytypes.

The extremes in thermal, mechanical, chemical and electronic properties of SiC allow the types and numbers of current and conceivable applications of this material to be substantial. However, a principal driving force for the current resurgence in interest in this material, as well as AlN and GaN, is their potential as hosts for high power, high temperature microelectronic and optoelectronic devices for use in extreme environments. The availability of thin film heterostructural combinations of these materials will substantially broaden the applications potential for these materials. The pseudomorphic structures produced from these materials will be unique because of their chemistry, their wide bandgaps, the availability of indirect/direct bandgap combinations, their occurrence in cubic and hexagonal forms and the ability to tailor the lattice parameters and therefore the amount of strain and the physical properties via solid solutions composed of the three components.

In this first reporting period, the P.I. and his coworkers have conducted studies in three primary areas of the grant: (1) development and application of computer codes

concerned with pseudomorphic structures, and specifically in the cBN-diamond binary as a model system; (2) the growth of GaN/AlN pseudomorphic heterostructures; and (3) the design and fabrication of a growth system for the deposition SiC/AlN/GaN pseudomorphic structures. The procedures, results and a discussion of these results and directions for future research are presented in the following sections.

II. The Role of Geometric Considerations in the Diamond-Cubic Boron Nitride Heteroepitaxial System

A. Introduction

Evidence of heteroepitaxial growth of Diamond on some faces of a cubic Boron-Nitride substrate was recently reported by Koizumi *et al* [1] and Yoshikawa *et al* [2]. This stimulated the examination of this system in terms of a general epitaxial criterion first obtained by Fletcher [3] and derived by other means and extended by Braun [4,5]. It is found that the reported observations of this system agree well with the reciprocal space considerations. It is conjectured that the rigidity of Diamond makes the agreement with the geometric matching requirement a strong necessary condition for epitaxy. This would enable the selection of candidate substrates for heteroepitaxy with Diamond.

This paper briefly reviews the principles of the interfacial energy considerations in terms of the Van der Merwe-Reiss rigid model [6,7] and follows a derivation given by Braun of an epitaxial criterion formulated in reciprocal space. It further reviews the reciprocal space and direct space consequences of the criterion. These considerations are then applied to the matching conditions of the low index like faces of Diamond and cubic Boron-Nitride as well as the mixed face pairs of Diamond {100}, {110}, {111}, {112}, {114} and {120} on BN {221} and Diamond {110} on the BN{120} face, Diamond {100} on BN{110}, and Diamond {100}, {110} and {111} on the BN{112} faces. Some unique aspects of the Diamond {100}, BN{221} pair are highlighted.

B. The Epitaxial Criterion

Several models which give the energy of the bicrystal subject to various approximations have been used to predict epitaxial orientations or interfacial structure [3,6,7,8,9,10]. Inherent to them is the assumption that epitaxial orientations minimize the Gibbs free energy of the system, a condition usually approximated by minimizing the bicrystal energy itself.

In the geometric limit both components of the bicrystal are considered rigid, retain their bulk lattice structures and parameters and are in contact at a single interfacial plane. On either side of the interface each component crystal presents a crystal plane with unique translational and rotational symmetries. The periodicities are described by infinite sets of wave vectors which form the surface reciprocal lattices for each crystal face.

The interaction energy between individual interfacial overgrowth atoms (adatoms) and the substrate surface is assumed to be dependent on position and is given in Fourier form as the potential

$$V(x,y) = \sum_{\{\mathbf{q}\}} V_{\mathbf{q}} \exp(i\mathbf{q}\cdot\mathbf{r}) = \sum_{h,k=-\infty}^{\infty} V_{hk} \exp[i2\pi (hx+ky)] \quad (1)$$

where $\mathbf{q} = h\mathbf{a}_1^* + k\mathbf{a}_2^* \equiv \mathbf{q}_{hk}$ is a lattice translation vector of the substrate surface reciprocal lattice (defined by the condition $\mathbf{a}_i \cdot \mathbf{a}_j^* = 2\pi\delta_{ij}$) and h and k are required to be integers. In this expression, position in the substrate surface lattice is given by $\mathbf{r} = x\mathbf{a}_1 + y\mathbf{a}_2$.

An overgrowth island is constructed to contain $(2M+1) \times (2N+1)$ overgrowth lattice points. These are arranged as $2N+1$ rows of $2M+1$ points each, and are obtained by displacing a single (central) point by all the vectors in the set

$$\{\mathbf{r}_b = m\mathbf{b}_1 + n\mathbf{b}_2 : m = -M, \dots, 0, \dots, M; n = -N, \dots, 0, \dots, N\} \quad (2)$$

It is assumed here, that the origin of the overgrowth lattice is placed at a minimum of energy in the substrate potential, (eq. 1) and that this is also chosen as the origin of the substrate lattice. The energy scale is chosen in such a way that if every overgrowth atom lies at an exact minimum of the substrate, the total energy given by expression (1) will be zero. Any deviation from this exact matching situation (misfit then exists) yields an energy greater than zero. With this choice the energy is interpreted directly as *misfit energy*.

After summing individual energy contributions over all the atoms in the overgrowth island, the total interaction energy *per atom* for G overgrowth atoms is seen to be

$$V_{\alpha} = \frac{1}{G} \sum_{hk} V_{hk} \frac{\sin \pi(2M+1)p(h,k)}{\sin \pi p(h,k)} \cdot \frac{\sin \pi(2N+1)q(h,k)}{\sin \pi q(h,k)} \quad (3)$$

The rather distinctive sine expressions also occur in the standard derivation of the von Laue condition in x-ray crystallography, (see for example the text by Busch and Schade[11], or Kittel[12]) and are in fact obtained here in an analogous summation process.

The relationship between the pairs p, q and h, k is given by the expressions

$$p(h,k) = hr_{11} c_{\theta} + kr_{12} s_{\theta} \quad , \quad q(h,k) = hr_{21} s_{\theta} + kr_{22} c_{\theta} \quad (4a)$$

with θ the angle between b_1 and a_1 and

$$\begin{aligned} r_{ij} = b_i/a_j = (C_{bi}/C_{aj})r \quad , \quad r = b_{nn}/a_{nn} \quad , \quad i,j = 1, 2 \quad (4b) \\ c_{\theta} = \sin(\alpha-\theta)/\sin \alpha \quad , \quad s_{\theta} = \sin \theta/\sin \alpha \quad , \\ s_{\theta\beta} = \sin(\alpha-\beta-\theta)/\sin \alpha \quad , \quad c_{\theta\beta} = \sin(\beta+\theta)/\sin \alpha \end{aligned}$$

while r is termed the ratio of nearest neighbour distances, a_{nn} and b_{nn} , or simply the nearest neighbour ratio. This identifies with the atomic size ratio introduced by Bruce

e.a. [13]. Other quantities are the angles α and β , the substrate and overgrowth surface unit cell angles, and the lengths a_i and b_i , the lengths of the surface cell basis vectors.

Direct calculation of the transformation between the b_1, b_2 and a_1, a_2 systems shows that $p(h,k)$ and $q(h,k)$ are none other than the overgrowth reciprocal lattice coordinates of the substrate wave vector q_{hk} . The energy in the eq. (3) peaks sharply when p and q are integers. When this necessary condition is met the misfit energy is sharply minimized when the product of the sine terms and the resonating V_{hk} is negative. Translation of the origin of the overgrowth in the substrate unit cell to (x_0, y_0) introduces a factor $F^0 = \exp(iq_{hk} \cdot r_0) = \exp[i2\pi(hx_0 + ky_0)]$ and a factor of this type may be introduced to invert the sign (but implies displacement of the island).

This means that a translation vector of the substrate reciprocal lattice q_{hk} must coincide with a translation vector of the overgrowth reciprocal lattice, q^{pq} , where p and q are integers.

Hence, the condition

$$q_{hk} = q^{pq} \quad (5)$$

defines a *necessary* condition for an *ideal epitaxial configuration*. This is defined as an orientation and associated nearest neighbour ratio at which the interfacial misfit energy is minimized for a rigid system with these structures [6]. At equilibrium, systems with ideal lattice parameters will be found in the orientation yielding the least interfacial energy. This reciprocal space condition has previously been obtained from a different model by Fletcher [3]. It is analogous to the von Laue condition of crystallography.

Reciprocal lattice vectors in two dimensions propagate line wave fronts which coincide with rows of lattice points. The spacing of such rows of lattice points is given by the wavelengths of the propagation vectors, while the direction of the wave vectors

is perpendicular to the lattice rows. The spacing of the rows propagated by vector \mathbf{q}_{hk} is given by

$$\lambda_{hk} = \frac{2\pi}{|\mathbf{q}_{hk}|} = \frac{2\pi}{\sqrt{h^2\mathbf{a}_1^* \cdot \mathbf{a}_1^* + 2hk\mathbf{a}_1^* \cdot \mathbf{a}_2^* + k^2\mathbf{a}_2^* \cdot \mathbf{a}_2^*}} \quad (6)$$

In analogy to the zone law, it is always true that

$$h\mathbf{a}_1^* + k\mathbf{a}_2^* \perp k\mathbf{a}_1 - h\mathbf{a}_2 \quad (7)$$

Consequences of the coincidence of a pair of overgrowth and substrate reciprocal lattice vectors may be listed as follows:

- i) If the wave vectors are parallel, then so are the lattice rows they propagate. This means that when crystals are aligned in an ideal epitaxial orientation, lattice rows of substrate and overgrowth are aligned in parallel orientation.

When a pair of vectors is not parallel, the magnitude of the necessary angle of rotation is given by

$$\cos \theta_R = \frac{\mathbf{q}^{pq} \cdot \mathbf{q}_{hk}}{|\mathbf{q}^{pq}| |\mathbf{q}_{hk}|} \quad (8)$$

and the sense of the angle by the vector cross product.

- ii) The aligned lattice rows must have the same spacing. As $\mathbf{q}_{hk} = \mathbf{q}^{pq}$ it follows that

$$\lambda_{hk} = \lambda^{pq} \quad (9)$$

(This requirement is the analog of the Bragg condition of crystallography)

When the spacing is dissimilar, the misfit may be accommodated in several ways. If the crystal strains homogeneously (as in the case of pseudomorphic growth),

the matching may be one-dimensional, (atomic spacing along the rows is still unequal) or two-dimensional when both the perpendicular row spacing as governed by condition 5 and 9 and the atom positions along the rows match. Alternatively, misfit dislocations may be introduced to accommodate both orientational and dimensional mismatch by screw and edge misfit dislocation arrays respectively.

Two-dimensional coherency, requires that the epitaxial criterion is satisfied by *two non-colinear pairs* of substrate and overgrowth reciprocal lattice vectors [4,5].

Real systems might be expected to strain to achieve pseudomorphic structures, depending on the gain in interfacial energy compared to the cost in strain energy. The strains may be calculated directly from the reciprocal lattice, and a measure of the strain energy is provided by the strain energy density calculated from the strains and known plane stress elastic constants (suitable for thin films) calculated for the overgrowth orientation.

Another result of eq. (3) is a consequence of the value of the Fourier coefficient, V_{hk} . When a particular substrate wave vector q_{hk} resonates with the overgrowth vector q^{pq} , the contribution to the misfit energy is positive or negative depending on the sign of V_{hk} and of the product of sine-expressions. Additionally the total reduction in misfit energy achieved by a particular system is given by the sum of all the V_{hk} terms (with signs) which resonate in this fashion. This sum of Fourier coefficients active in a particular epitaxial orientation is a measure of the tendency to epitaxy [6]. An obvious generalization treats the substrate in the field of the overgrowth system as experiencing a misfit energy similarly expressible as a Fourier series as eqs. (1) and (3), but summed over the reciprocal lattice vectors of the overgrowth. The total misfit energy is then given by $\frac{1}{2}(V_a + V_b)$. Qualitatively, the magnitude of Fourier coefficients tends to decrease with order $(|h|+|k|, |p|+|q|)$ [14], so that the shorter the reciprocal lattice vectors which resonate, the likelier will be the actual occurrence of the particular epitaxial configuration. Also the higher the density of reciprocal lattice vectors which match in the two-dimensional reciprocal

space, the lower the misfit energy and the stronger the epitaxial tendency, although this must be qualified by the signs of the Fourier coefficients.

C. Special Considerations in Covalent Polyatomic Systems

The expression (1) is given in its simplest form, and to be useful for systems of several atom types, or bonding states, a series for each atom type represented in the overgrowth for V_A , and similarly, for each substrate species a series for V_B , should be constructed. Additionally, localization of the bond in the unit cell may be achieved by careful choice of Fourier coefficients. These will further complicate the misfit energy expressions eq. (3), but the epitaxial criterion remains a *necessary* condition.

The geometric emphasis here does not require any values for these Fourier coefficients. In the following discussion, the three quality factors, strain energy density, order of the Fourier term and the degree of coincidence of reciprocal lattice points are used to order the possible epitaxial configurations.

D. Application to the Diamond - BN_{cub} System

In order to apply the epitaxial criterion it is necessary to construct the reciprocal spaces of both the overgrowth and substrate surface lattices. We have generally chosen primitive surface lattices to avoid complications with structure factors due to non-primitive unit cell constructions. Needed are surface unit cell parameters (angles and lengths obtainable from Table I) and the scale parameter, usefully given as the ratio of nearest neighbour distances in the bulk (eq 4b), was chosen as $r = 0.986489$ for this study.

Two-dimensional plane stress elastic constants suitable to the overgrowth orientation are required when strain energy densities and the strains of one-dimensional matching conditions are calculated. These boundary conditions require the upper surface of the overgrowth to be free of stresses in the normal direction, $\sigma_{zi} = \sigma_{iz} = 0$, $i = x, y, z$.

Table I: This Table shows the unit cell choices for several low-index planes in the underlying structure of both Diamond and BN_{cub}. Lattice Parameters are 3.56685Å and 3.6157Å for Diamond and BN_{cub} resp. [15]

h k l	a ₁ or b ₁	a ₂ or b ₂	α or β
1 0 0	$\frac{1}{2}[0 \bar{1} \bar{1}]$	$\frac{1}{2}[0 1 \bar{1}]$	90
1 1 0	$\frac{1}{2}[1 \bar{1} 0]$	$[0 0 \bar{1}]$	90
1 1 1	$\frac{1}{2}[1 \bar{1} 0]$	$\frac{1}{2}[1 0 \bar{1}]$	60
1 2 0	$[0 0 \bar{1}]$	$\frac{1}{2}[\bar{2} 1 \bar{1}]$	65.9
1 1 2	$\frac{1}{2}[1 \bar{1} 0]$	$[1 1 \bar{1}]$	90
1 1 4	$\frac{1}{2}[1 \bar{1} 0]$	$[2 2 \bar{1}]$	90
2 2 1	$\frac{1}{2}[1 \bar{1} 0]$	$\frac{1}{2}[1 1 \bar{4}]$	90

We have used the program LATUSE/SARCH by van Hove and Hermann [14] to determine the surface cell structures, and our own program ELCON to transform elastic constants to the required plane and apply the plane stress boundary conditions. The reciprocal space searches were carried out with an interactive version of the program ORPHEUS [4]. Both programs ELCON and ORPHEUS are available for MSDOS and Macintosh computers.

The ORPHEUS program produces scaled plots of the substrate and overgrowth reciprocal lattices and interactively leads the user through a construction analogous to the Ewald construction of crystallography. By selecting a substrate reciprocal vector, q_{hk} , and drawing a circle, centred at the origin, through its end, the locus of the end-point of the vector as it is rotated through 360° is constructed. Any overgrowth reciprocal lattice point which lies on this circle describes an overgrowth reciprocal lattice translation vector, q^{pq} equal in length to q_{hk} . The angle between q^{pq} and q_{hk}

determines the orientation angle, this being the angle θ_R through which the overgrowth must be rotated to come into epitaxial orientation with the substrate. The strains needed to bring a vector nearly on the circle into coincidence and the associated energy are calculated from the components of the selected vectors. The selection of substrate and overgrowth vectors, and the subsequent calculation of angles of rotation, strains and strain energies are done interactively with the Orpheus program. Plots showing the subsequent reciprocal lattices in coincidence are produced by the program, from which quality judgements relating the density of points which coincide with efficiency of the epitaxial matching may be made.

As both Diamond and BN_{cub} share the geometry of the zincblende structure a single set of unit cell descriptions is given for the planes we considered.

The results are summarized in Table II, where the matching conditions which give lowest strain energy in several plane combinations are given. For like planes an isotropic extensive strain of 1.37% introduces two-dimensional pseudomorphy with zero misfit energy and a strain energy density of $2.2 \times 10^9 \text{erg cm}^{-3}$, only twice as high as the one-dimensional matching case, (typically, $1.09 \times 10^9 \text{erg cm}^{-3}$), but with increased misfit energy.

Several partially matching cases are distinguished in Table II, and these form a hierarchy ordered by the density of reciprocal lattice points that are paired in both overgrowth and substrate. Of lowest misfit energy is the 2-dimensional pseudomorphic case, in which there is perfect continuation of the substrate lattice into the overgrowth. This case occurs only for like planes. The Diamond{100} on BN_{cub} {100} case is presented as an illustration in Figure 1. A less favourable case is indicated by P-2, in which all overgrowth reciprocal lattice vectors match substrate vectors, but some substrate vectors do not have counterparts in the overgrowth reciprocal lattice. This occurs only in the epitaxial configuration in which Diamond{100} grows on BN_{cub} {221}, shown in Figure 2. The cases indicated by (2) have coincidence matching in at least one direction, where some overgrowth reciprocal

Table II: Epitaxial orientations for various combinations of dissimilar planes in which the geometric relationship which minimizes strain energy are shown for low-index planes. Diamond forms the overgrowth in all cases.

Planes: BN _{cub} Diamond	Lattice Directions: Parallel rows Zero Misfit Direction (S: Secondary - Notes 1) (BN: Boron Nitride, C:Diamond)	Strains (e _x e _y) (e _x e _y g _{xy} if g _{xy} ≠0) (Notes 2)	Strain Energy density (×10 ⁹ erg cm ⁻³)	Type (Notes 3)	
Like Planes:					
h k l h k l	$\begin{cases} \text{B} & [u \ v \ w] \\ \text{C} & [u \ v \ w] \end{cases}$	$\begin{cases} [U \ V \ W] \\ [U \ V \ W] \end{cases}$	1.37% -0.01%	1.09 [†]	P1
	S: $\begin{cases} \text{B} & [U \ V \ W] \\ \text{C} & [U \ V \ W] \end{cases}$	$\begin{cases} [u \ v \ w] \\ [u \ v \ w] \end{cases}$	1.37% 1.37%	2.20	P
Unlike Planes:					
2 2 1 1 0 0	$\begin{cases} \text{B} & [\bar{1} \ \bar{1} \ 4] \\ \text{C} & [0 \ \bar{1} \ 1] \end{cases}$	$\begin{cases} [1 \ \bar{1} \ 0] \\ [0 \ \bar{1} \ \bar{1}] \end{cases}$	1.37% -0.01%	1.09	P1
	S: $\begin{cases} \text{B} & [1 \ \bar{1} \ 0] \\ \text{C} & [0 \ \bar{1} \ \bar{1}] \end{cases}$	$\begin{cases} [\bar{1} \ \bar{1} \ 4] \\ [0 \ \bar{1} \ 1] \end{cases}$	1.37% 1.37%	2.20	P-2
1 1 0	$\begin{cases} \text{B} & [\bar{1} \ \bar{1} \ 4] \\ \text{C} & [0 \ 0 \ 1] \end{cases}$	$\begin{cases} [1 \ \bar{1} \ 0] \\ [1 \ \bar{1} \ 0] \end{cases}$	1.37% -0.16%	1.09	P1
1 1 0	$\begin{cases} \text{B} & [1 \ \bar{3} \ 4] \\ \text{C} & [1 \ \bar{1} \ 2] \end{cases}$	$\begin{cases} [11 \ \bar{7} \ \bar{8}] \\ [1 \ \bar{1} \ \bar{1}] \end{cases}$	2.15% 1.00% 3.25%	6.57	P1
1 1 1	$\begin{cases} \text{B} & [\bar{1} \ \bar{1} \ 4] \\ \text{C} & [\bar{1} \ \bar{1} \ 2] \end{cases}$	$\begin{cases} [1 \ \bar{1} \ 0] \\ [1 \ \bar{1} \ 0] \end{cases}$	1.37% -0.11%	1.09	P-1
	S: $\begin{cases} \text{B} & [1 \ \bar{3} \ 4] \\ \text{C} & [0 \ \bar{1} \ 1] \end{cases}$	$\begin{cases} [11 \ \bar{7} \ \bar{8}] \\ [2 \ \bar{1} \ \bar{1}] \end{cases}$	-12.2% 1.37%	86.8	(2)

Table II: (Cont):

Epitaxial orientations for various combinations of dissimilar planes in which the geometric relationship which minimizes strain energy are shown for low-index planes. Diamond forms the overgrowth in all cases.

Planes: BN _{cub} Diamond		Lattice Directions: Parallel rows Zero Misfit Direction (S: Secondary - Notes 1) (BN: Boron Nitride, C: Diamond)		Strains (e _x e _y) (e _x e _y g _{xy} if g _{xy} ≠0)	Strain Energy density (×10 ⁹ erg cm ⁻³)	Type (Notes 3)	
2 2 1	1 1 2	{	B [1̄ 1̄ 4]	[1 1̄ 0]	1.37%	1.13	P1
		C [1̄ 1̄ 1]	[1 1̄ 0]	-0.06%			
		S: {	B [1 3̄ 0]	[1 1 4̄]	1.37%	1.35	(2)
		C [1 1̄ 0]	[1 1 1̄]	-0.68%			
1 1 2		{	B [1 1̄ 0]	[1 1 4̄]	1.37%	1.13	(1)
		C [1̄ 1̄ 1]	[1 1̄ 0]	-0.06%			
1 1 4		{	B [1̄ 1̄ 4]	[1 1̄ 0]	1.37%	1.09	P1
		C [2 2 1̄]	[1 1̄ 0]	-0.02%			
1 1 4		{	B [1 1̄ 0]	[1 1 4̄]	1.37%	1.09	(1)
		C [2 2 1̄]	[1 1̄ 0]	-0.02%			
1 2 0		{	B [1 3̄ 4]	[11 7̄ 8̄]	-0.06%	0.024	P1
		C [2 1̄ 3̄]	[6 3̄ 5̄]	-0.13% -0.20%			
		S: {	B [3 2̄ 2̄]	[2̄ 7̄ 10̄]	-2.86%	4.94	(2)
		C [2̄ 1 2̄]	[4 2 5̄]	1.37%			

Table II: (Cont):

Epitaxial orientations for various combinations of dissimilar planes in which the geometric relationship which minimizes strain energy are shown for low-index planes. Diamond forms the overgrowth in all cases.

Planes: BN _{cub} Diamond		Lattice Directions: Parallel rows Zero Misfit Direction (S: Secondary - Notes 1) (B: Boron Nitride, C:Diamond)		Strains (e _x e _y) (e _x e _y g _{xy} if g _{xy} ≠0) (Notes 3)	Strain Energy density (×10 ⁹ erg cm ⁻³)	Type (Notes 3)
120	110	{B C	{[00 $\bar{1}$] [1 $\bar{1}$ 2]	{ $[\bar{2}$ 10] [1 $\bar{1}$ $\bar{1}$]	{-1.21% -0.56% -1.82%	2.06 P1
	110	{B C	{[2 $\bar{1}$ 0] [1 $\bar{1}$ 0]	{[00 $\bar{1}$] [00 $\bar{1}$]	{-0.14% 1.37%	0.99 (1)
		S:{B C	{[2 $\bar{1}$ $\bar{3}$] [1 $\bar{1}$ $\bar{2}$]	{ $[\bar{6}$ 35] [$\bar{1}$ 1 $\bar{1}$]	{6.85% 1.37%	29.8 (2)
110	100	{B C	{[001] [0 $\bar{1}$ 1]	{[1 $\bar{1}$ 0] [0 $\bar{1}$ $\bar{1}$]	{1.37% -0.01%	1.09 P1
		S:{B C	{[1 $\bar{1}$ 0] [0 $\bar{1}$ $\bar{1}$]	{[00 $\bar{6}$] [01 $\bar{1}$]	{1.37% -4.4%	12.4 (2)
112	100	{B C	{[$\bar{1}$ $\bar{1}$ 1] [0 $\bar{1}$ 1]	{[1 $\bar{1}$ 0] [0 $\bar{1}$ $\bar{1}$]	{1.37% -0.01%	1.09 P1
		S:{B C	{[1 $\bar{1}$ 0] [0 $\bar{1}$ $\bar{1}$]	{[11 $\bar{1}$] [01 $\bar{1}$]	{1.37% -0.68%	1.35 (2)
112	110	Nothing within a strain of 4%				
112	111	Nothing within a strain of 8%				

Notes on Table II:

1. Secondary matching conditions (S) refer to directions in the overgrowth and substrate which match in addition to those which already resulted in the one-dimensional coherency. These increase the type of matching to two-dimensional when the new strains are applied.
2. The cartesian coordinates in which strains are expressed are chosen with the x-direction parallel to the unit cell vector b_1 and the z-direction perpendicular to the plane. Additionally, the y-direction is perpendicular to both, and the vectors form a right-handed system.
3. Types of matching are identified as follows:

2-dimensional match:

- P: exact continuation of the substrate structure, including interfacial lattice parameters, as Pseudomorphic (P). (Applies to both reciprocal and direct spaces)
- P-2: all overgrowth reciprocal lattice points match exactly to substrate points, but some substrate points do not have overgrowth counterparts
- (2): refers to the general case of two-dimensional coherency with coincidence in either the Frank or Bollmann senses, but excludes the pseudomorphic case. 1-dimensional pseudomorphism, in the P^1 -sense may still be present.

1-dimensional match:

- P^1 : exact matching of all reciprocal lattice points of the overgrowth with all of those of the substrate in one direction in reciprocal space. Direct space lattice rows are equally spaced and parallel, but lattice positions along the rows are not in coincidence.
 - P-1: all overgrowth reciprocal lattice points coincide with substrate points, but not all substrate points have counterparts in the overgrowth, one-dimensionally.
 - (1): some overgrowth and substrate points fail to match, while overgrowth reciprocal lattice points periodically match substrate points. Coincidence in the Frank or Bollmann senses occurs, but one-dimensionally.
-

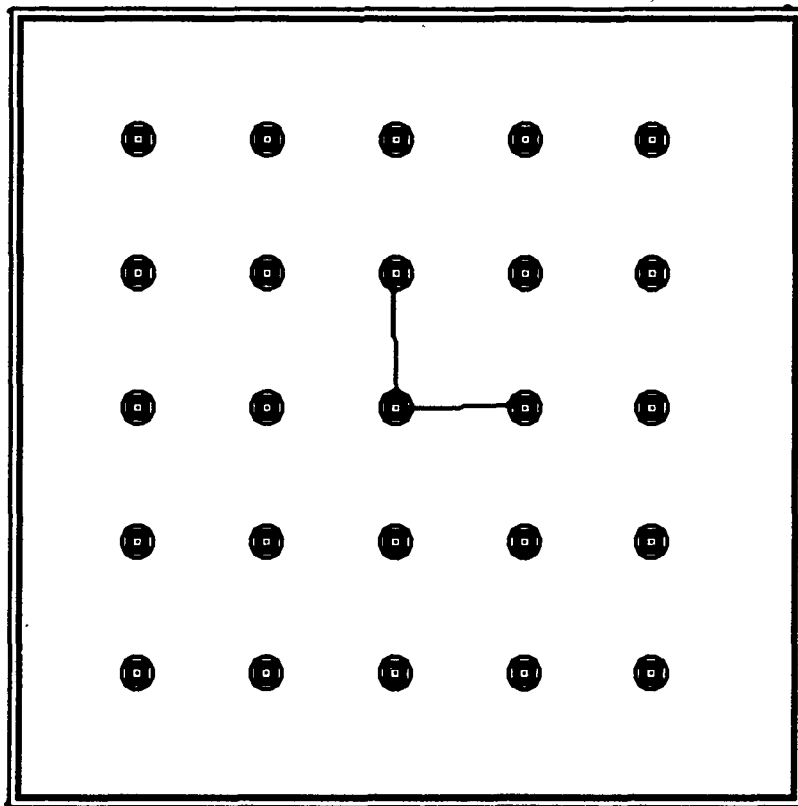


Figure 1: Superimposed reciprocal spaces of the Diamond and cubic Boron Nitride {100} faces showing full pseudomorphism (P) after isotropic strain of 1.37%.

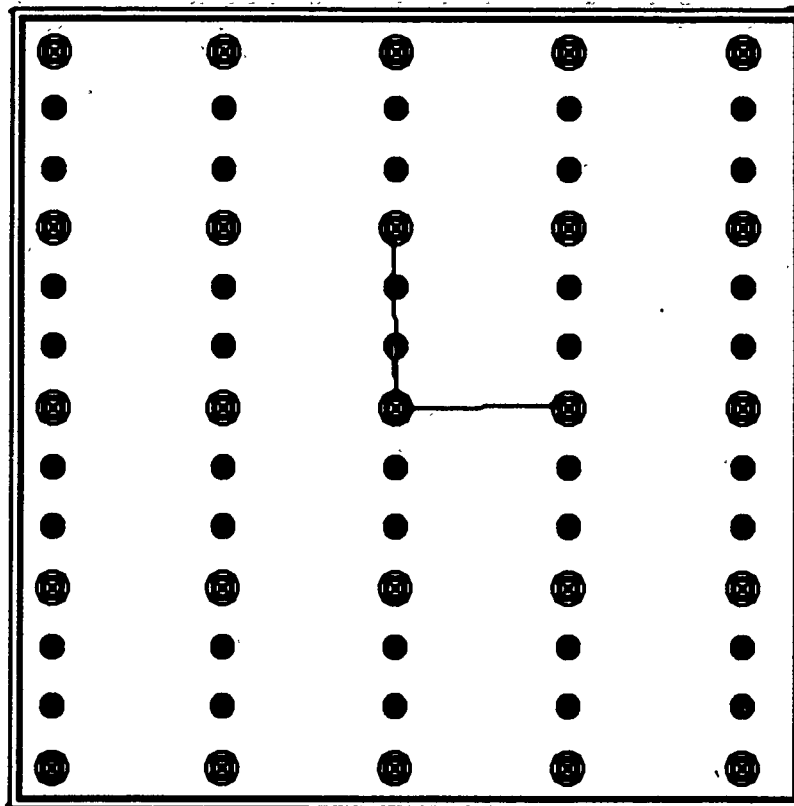


Figure 2: Superimposed reciprocal lattices of the Diamond {100} and cubic Boron Nitride {221} surfaces, showing the coincidence matching after isotropic 1.37% strain. This matching configuration is referred to as P⁻² in the Table 2 and in the text.

The symbols : \odot indicate matched overgrowth and substrate points, \bullet mean substrate reciprocal lattice points which do not have partners in the overgrowth.

lattice vectors do not have matched counterparts in the substrate, and some substrate points do not have counterparts in the overgrowth. An example is presented in Figure 3.

A similar hierarchy of one dimensional matching cases is also distinguished in Table II.

Of most interest is the Diamond {100} matching with the $\text{BN}_{\text{cub}}\{221\}$. Here isotropic strain of 1.37% introduces two-dimensional coincidence, but with irregular matching in the Diamond $[0\ 1\ \bar{1}]$ direction when parallel with the $\text{BN}_{\text{cub}}[1\ 1\ \bar{4}]$ direction. These are the same strains as for the pseudomorphic Diamond{100} // $\text{BN}_{\text{cub}}\{100\}$ case. No other low-index plane combination of unlike planes yielded 2-dimensional coherency of this quality.

The results may be summarized as showing that the two-dimensional pseudomorphic matching (Figure 1) is only a little more expensive in strain energy than one-dimensional pseudomorphy in like planes. The second best matching possibility is the Diamond{100} on $\text{BN}_{\text{cub}}\{221\}$ case (Figure 2), identical in strain energy to pseudomorphic cases, but with increased misfit energy. The realization of either or both of {100} or {221} with the {221} substrate will clearly depend on growth conditions. Of other unlike pairs, the Diamond{100} on $\text{BN}_{\text{cub}}\{112\}$ configuration (Figure 3) has a two dimensional configuration with a strain energy density of $1.35 \times 10^9 \text{erg cm}^{-3}$ comparable to the one dimensional case. However, this is only a rather high order coincidence match in which every fifth substrate reciprocal lattice point coincides with every second overgrowth point resulting in a high misfit energy, better than one dimensional matching, but somewhat unfavourable when compared to the possibility of pseudomorphic Diamond{112} on $\text{BN}_{\text{cub}}\{112\}$. Other unlike planes do not have the possibility of two dimensional coherency within such a low energy so making it unlikely that unlike planes will grow epitaxially.

The experiments reported by Koizumi *et al* [1] and Yoshikawa *et al* [2] indicate results which agree very well with these geometric considerations. In the

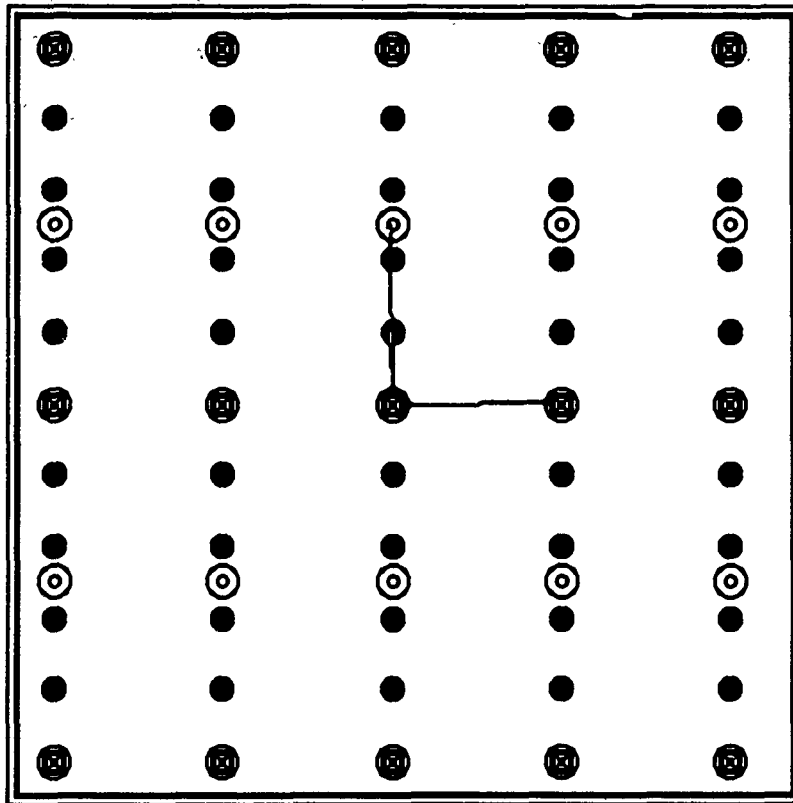


Figure 3: Superimposed reciprocal lattices of the Diamond {100} and cubic Boron Nitride {112} surfaces, showing the coincidence matching after strain of $\epsilon_{xx} = 1.37\%$, $\epsilon_{yy} = -0.68\%$. This matching configuration is an example of the type (2) in the Table 2 and in the text.

The symbols : ⊠ indicate matched overgrowth and substrate points, \bullet mean substrate reciprocal lattice points which do not have partners in the overgrowth, ⊙ mean overgrowth points which do not have partners in the substrate.

low-index substrates diamond prefers to grow in pseudomorphic arrangement to the alternative but higher index coincidence planes. This situation has appeared to reverse in the $\text{BN}_{\text{cub}}\{221\}$ case, where Diamond preferred the low-index $\{100\}$ orientation to a final pseudomorphic $\{221\}$ configuration. The experiment could not show conclusively that the original configuration differed from $\{221\}$ however, while the experimental indications appear to be that the interface conforms to Diamond $\{221\}$, while away from the interface the final orientation becomes $\{100\}$.

E. Conclusions

The Diamond- BN_{cub} system appears to agree with the geometric considerations as expressed in the reciprocal lattice criterion.

Low index like planes have been observed to grow pseudomorphically experimentally, and the geometrically derived low required strain of 1.37% from bulk parameters is consistent. The unlike epitaxial configuration which pairs Diamond $\{100\}$ with $\text{BN}_{\text{cub}}\{221\}$ yields two-dimensional coincidence with the same small strain, and is favoured above other low-index mixed configurations in this way. The reason for observed $\{100\}$ growth as opposed to $\{221\}$ growth of the diamond is probably due to surface energy properties and conditions during growth, although as was pointed out, the experiment itself is ambiguous about the possibility that the $\{221\}$ orientation is actually retained in the interface, transforming into a $\{100\}$ orientation some distance away from the interface.

The rigidity of diamond suggests that geometric criteria are particularly suitable as a tool for selecting candidate substrate planes, particularly important where structures of dissimilar types are considered as substrate candidates. The reciprocal lattice provides clarity where considerations with atomic rows tend to be clouded by details of atomic positions.

Candidate surfaces of other and dissimilar structures will be sought with these techniques.

III. AlN/GaN Multilayer and Pseudomorphic Heterostructures

A. Introduction

Bandgap engineering in the range of 3.4–6.2 eV can be achieved either by solid solutions or by layered structures of GaN and AlN. So far only AlGa_N solid solutions have been studied [17-19]. The superlattices are favored for several reasons. As has been shown for the GaAs/GaAlAs system, [20-237] optoelectronic devices using multi-quantum well structures instead of solid solutions exhibit lower threshold current density, lower non-radiative recombination rate, narrower emission spectra and reduced sensitivity to temperature. The lattice parameter mismatch between AlN and GaN is only 3.5%, thus layered structures of these two materials offer a way of producing high quality, low dislocation density GaN- and/or AlN-based materials and devices. To our knowledge, layered structures of these two materials have not been produced prior to this investigation.

B. Growth Procedure

Growth studies were conducted on (0001)-oriented α -SiC (6H polytype) and (0001) oriented epitaxial quality sapphire substrate wafers, both of which have a hexagonal structure. All substrates were cleaned to remove organic and metallic contaminants using the following sequence of chemicals, temperatures and times: 1:1:5 solution of HNO₃:H₂O₂:H₂O at 75°C for 5 min, DI water rinse for 1 min, 1:1:5 solution of HCl:H₂O₂:H₂O at 75°C for 5 min and DI water for 5 min. The α -SiC wafers were subsequently oxidized in flowing dry oxygen at 1200°C for 1.5 hrs in order to consume an \approx 50 nm thick surface layer of the wafer which contained polishing damage. To remove this oxide layer the substrates were etched for 1 min in 49% HF and rinsed in DI water prior to loading into the MBE system. These last two chemical procedures were also performed on the sapphire wafers. All substrates were then mounted on a standard 3 inch molybdenum block with indium which provided both good adherence and thermal contact.

The substrates underwent an initial low temperature ($\approx 70^\circ\text{C}$) outgasing in the load lock followed by slow heating in the transfer tube to a maximum of 900°C with a dwell time of 30 min at this temperature. After cooling, the samples were introduced into the growth chamber and examined by reflection high energy electron diffraction (RHEED) using a 10 kV beam. The resulting RHEED patterns on both the α -SiC and sapphire substrates showed Kikuchi lines indicative of good crystalline quality.

Prior to growth, the substrates were heated to the desired deposition temperature and subsequently exposed to a flux of plasma activated nitrogen species for about 5 min. No change in the RHEED pattern occurred as a result of this procedure. Following the stabilization of temperatures and fluxes, a 140 nm thick GaN buffer layer was grown followed by 20 to 200 periods of AlN/GaN layers having the thickness for a given deposition in the range of 1.5–40 nm. The growth conditions are summarized in Table III.

TABLE III. Growth conditions

Nitrogen pressure	1×10^{-4} Torr
Microwave power	50 W
Gallium temperature	990°C
Aluminum temperature	1120°C
Substrate temperature	$400\text{--}750^\circ\text{C}$
Growth rate:	
GaN	≈ 2.5 nm/min
AlN	≈ 1.6 nm/min
GaN buffer layer thickness	140 nm
Period thickness	1.5–40 nm
Number of periods	20–200
Total growth time	6–7 hrs

After the total growth sequence was completed, the gallium and aluminum cells and the substrate were cooled, while the nitrogen source remained active. This source was turned off and the growth chamber returned to UHV conditions once the substrate temperature was below 400°C . The sample was again evaluated with RHEED to

determine the crystal structure and to obtain an initial estimate of the film quality. For a detailed description of the experimental procedures, the reader is referred to Refs. 24 and 25.

C. Chemical Analysis

Scanning Auger microprobe (SAM) (JEOL JAMP-30) analysis was used to determine the presence of impurities and the nominal compositions of the AlN and GaN layers. Auger spectra taken from the untreated surface showed oxygen and carbon surface contamination due to exposure of the film to the atmosphere. Figure 4 shows an Auger depth profile taken from a sample with 20 AlN/GaN double layers. The layers of each material were 10 nm thick. The profile indicates well defined layers. The samples with thicker layers also showed well defined and sharp interfaces. The quality of the interfaces could not be confirmed by SAM in the case of very thin multilayers, since the escape depth for Auger electrons is about 4–5 nm and because the depth resolution of the sputtering process, which roughens the surface, is in the same range. The Auger spectra presented in Figure 5 were taken from the fourth AlN and the fifth GaN layers of the sample noted in Figure 4. The spectra indicate nominal AlN and GaN compositions and some mixing of Ga and Al in AlN and GaN layers, respectively. A small amount of interfacial mixing may be present; however, TEM observations (see below) revealed well defined layers and thus indicate that the Auger data exaggerate this phenomenon for the reasons stated above. There is also a trace of oxygen contamination which decreased with the distance from the surface. As such, the oxygen peak may, at least partially, be due to the transfer of surface contaminants to the exposed material by ion beam sputtering. No other contaminants were observed within the resolution of the instrument (typically ≈ 0.1 at. %).

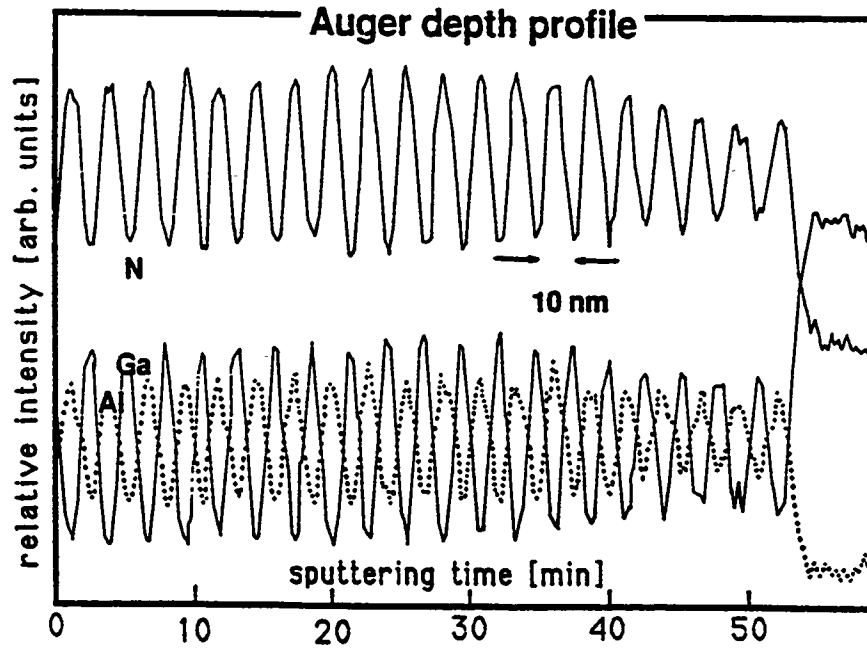


Figure 4. Auger depth profile taken from a sample with 20 AlN/GaN double layers. The layers of each material were 10 nm thick.

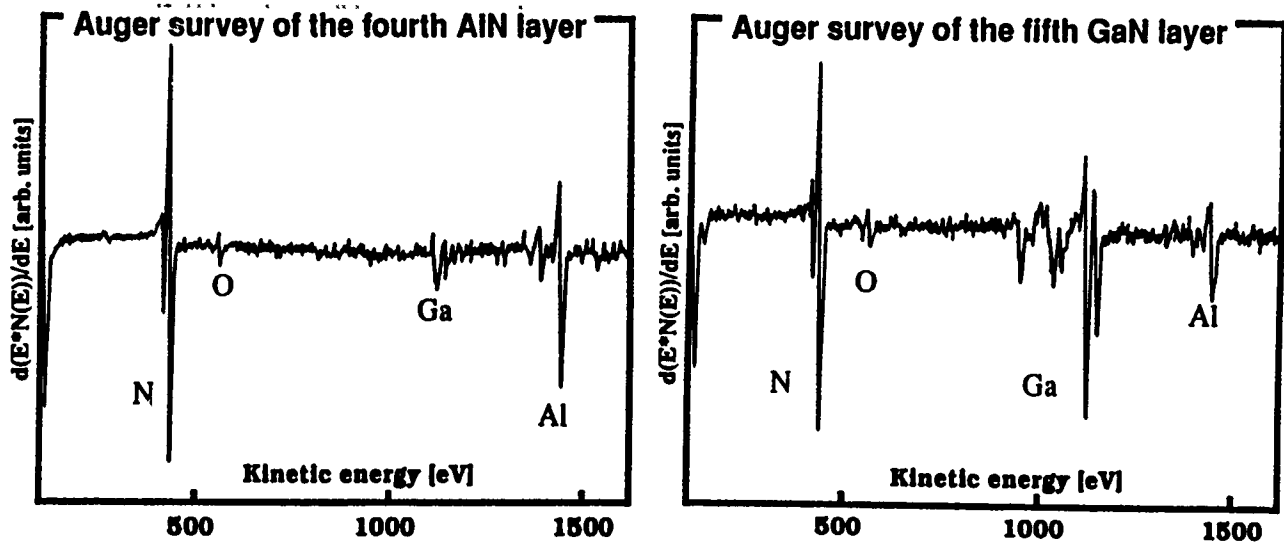


Figure 5. Auger spectra taken from the fourth AlN and fifth GaN layers of the sample noted in Figure 4. The apparent mixing of Al in GaN and Ga in AlN is probably an artifact (see text). Spectra indicate a trace of oxygen contamination.

D. Structural and Microstructural Analyses

X-ray Rocking Curves. The AlN/GaN layered structures were subsequently analyzed by x-ray diffractometry. The $\text{CuK}\beta$ line was used instead of filtered $\text{CuK}\alpha$ one to obtain a truly monochromatic x-ray line and, therefore, unambiguous determination of the AlN/GaN period and the crystalline quality of the superlattices produced in each deposition. The spectra were obtained around the expected (0002) reflections for "bulk" AlN and GaN.

A perusal of Figure 6 reveals that the diffraction spectra of the layered structures are much more complex than those for bulk crystals and single thin films. This is to be expected, since the lattice parameters in the direction normal to the layers (in our case (0001)) are different for AlN and GaN. Moreover the lattice parameters perpendicular to the surface depend upon the distortion of the lattice caused by the interlayer strain, and, as such, the diffraction peaks appear at different positions than one would expect from the bulk properties of the materials. The layered structure also introduces additional periodicity in the growth direction which is revealed in the diffraction spectra as well. Finally, the diffraction spectra usually contain a peak from the substrate or the buffer layer which is often much stronger than the superlattice peaks. These superimposed peaks are convenient for the determination of the strain in the layers[27, 28] but make diffraction spectra even more complicated and difficult to read.

Figures 6(a1-a6) show the evolution of the diffraction peaks as a function of decreasing AlN/GaN bilayer periodicity, P, which is given as

$$P = t_{\text{AlN}} + t_{\text{GaN}} \quad (1)$$

where t_{AlN} and t_{GaN} are the respective thicknesses of the individual layers of AlN and GaN. Each spectrum shows the (0002) diffraction peak from the GaN buffer layer and the zero order superlattice peak (marked "0"), which represents the average vertical lattice parameter of the superlattice, and associated satellite peaks (marked

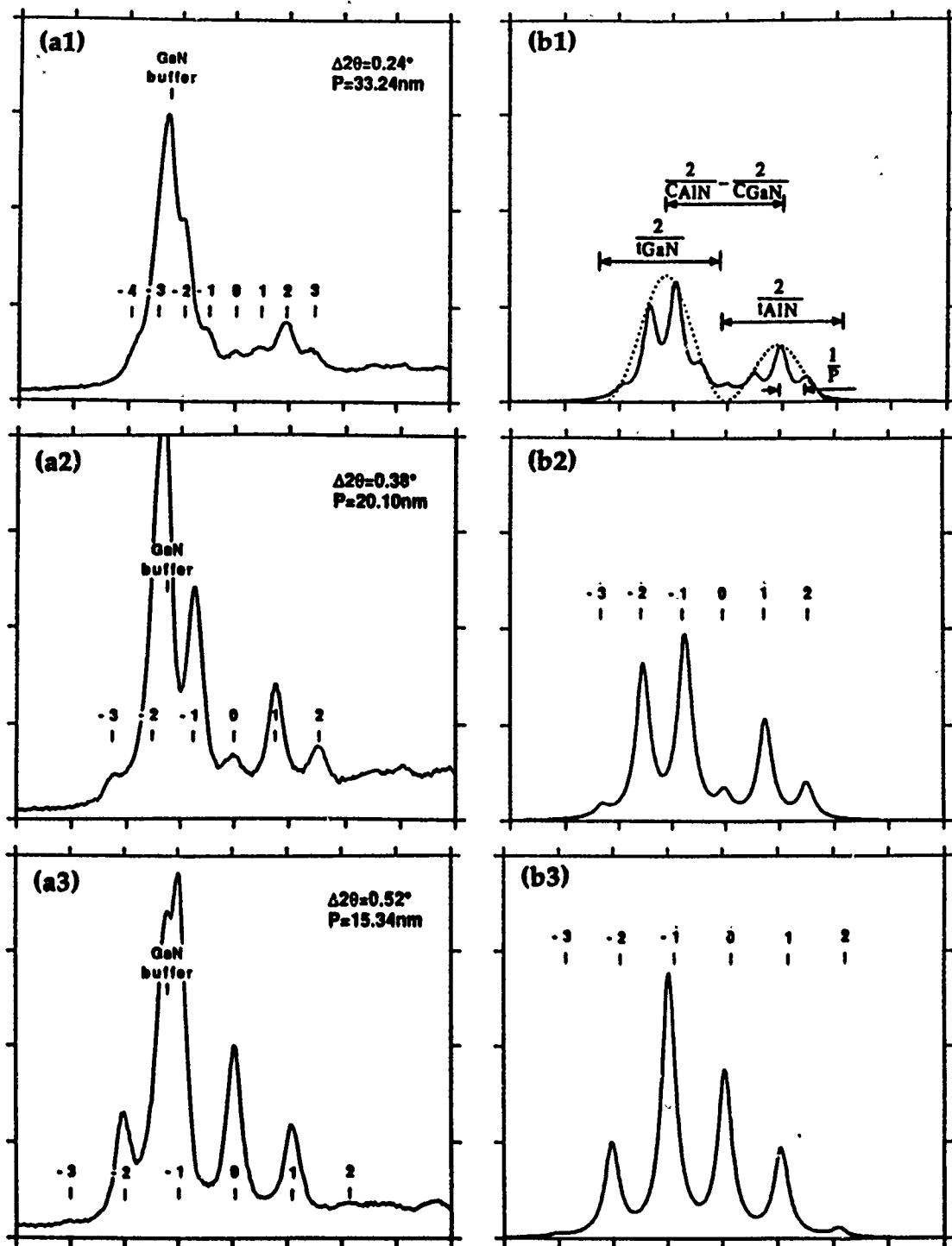


Figure 6. (a) X-ray diffraction spectra of the samples with different periodicities. Each pattern is characterized by the (0002) peak from the GaN buffer layer (marked by "GaN buffer") and a zero-order peak from AlN/GaN layers at $2q = 32^\circ$ (marked by "0") with satellite peaks around it. An angular spacing, $D2q$, of satellite peaks and a calculated bilayer period, P , is given for each spectrum. (b) Diffraction spectra after the subtraction of the GaN buffer layer peak and the overall background. Figure (b1) illustrates the use of the spectra for the determination of different parameters (see text).

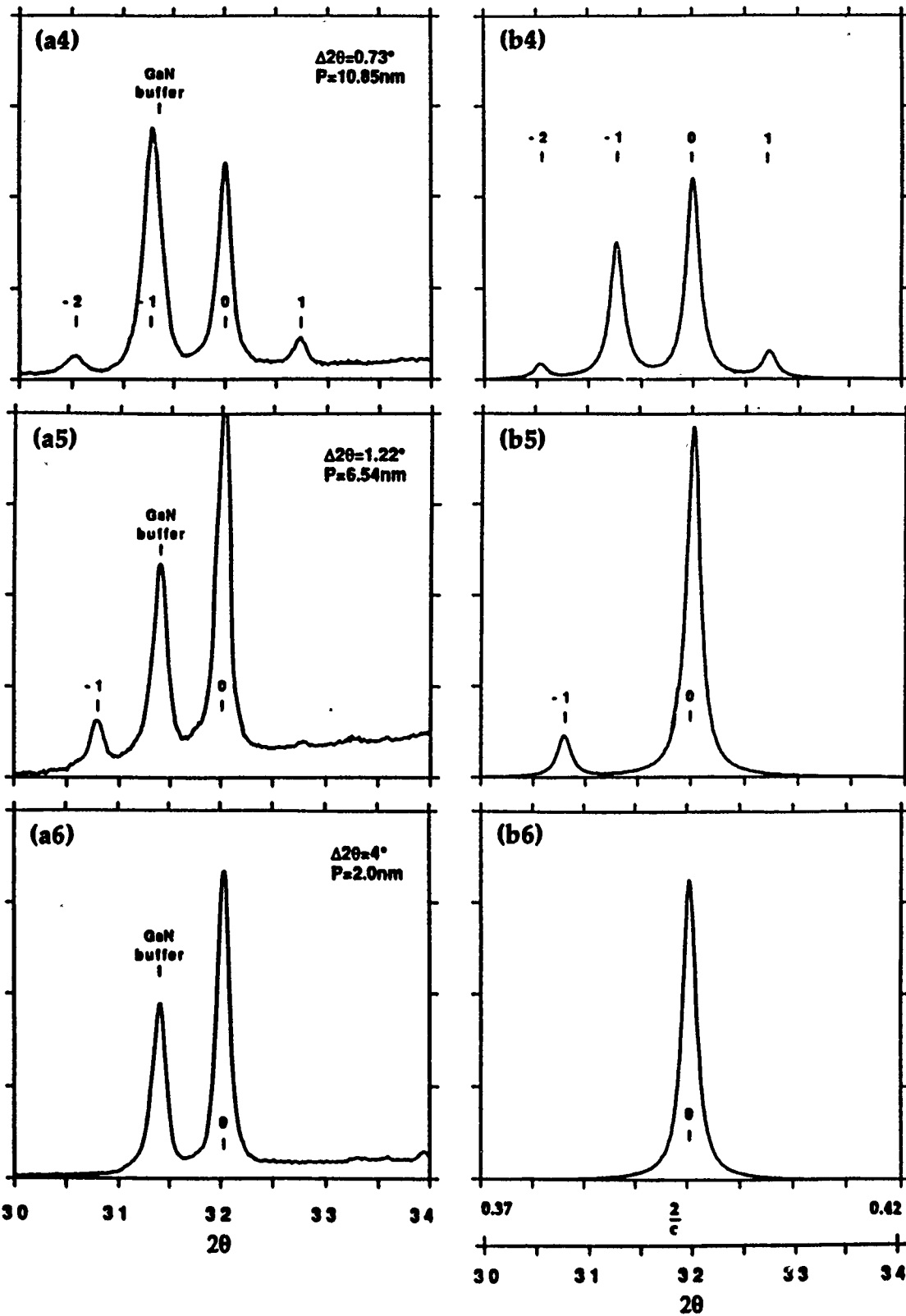


Figure 6. Continued

from -4 to 3). The buffer layer peak is superimposed on the latter peaks making the diffraction from the superlattice unclear. As such, each spectrum in Figure 6(a1-a6) was fitted with a sum of Lorentzian peaks followed by the subtraction of both the buffer layer peak and the overall background, which made the evolution of the peaks with the change of superlattice period easier to visualize. The resulting spectra are shown in Figure 6(b1-b6). In this latter set of spectra, the x-ray intensities are plotted as a function of $2/c$, where c is the lattice parameter perpendicular to the surface. This is convenient for measuring parameters (P , t_{AlN} , t_{GaN} , c_{GaN} , c_{AlN}) directly from the spectra.

A representative diffraction spectrum having marked parameters characteristic of a superlattice produced in this study is shown in Figure 6(b1). Several parameters can be determined, as indicated, by measuring reciprocal distances on the spectrum. The periodicity of the superlattice, P , is inversely proportional to the angular spacing of the satellite peaks. The values of t_{AlN} and t_{GaN} can be estimated from the widths of the envelopes (dotted curves) of the AlN and GaN sets of peaks. The perpendicular lattice parameters of the two materials in the individual layers are measured from the angular positions of the envelopes. Finally, the strain in the layered structure can be estimated by comparing the angular positions of the buffer layer peak with the superlattice peaks.

Figures 6(b1) and 6(b2) show two almost completely separated sets of superlattice peaks, each of which represents one of the two materials. Since the envelope widths of the two materials are proportional to $\frac{1}{t_{\text{AlN}}}$ or $\frac{1}{t_{\text{GaN}}}$ and their separation scales with $\frac{1}{c_{\text{AlN}}} - \frac{1}{c_{\text{GaN}}}$, we have the following condition for the two sets of peaks, taken around the (0002) pole, to be well separated:

$$\frac{2}{c_{\text{AlN}}} - \frac{2}{c_{\text{GaN}}} > \frac{1}{t_{\text{AlN}}} + \frac{1}{t_{\text{GaN}}}. \quad (2)$$

For example, if we assume that the lattice parameter perpendicular to the surface for each material has the same value as the bulk (as will be seen later, this is a reasonable assumption for thick layers) and take t_{AlN} equal to t_{GaN} , both sets of peaks are well separated for $P > 28$ nm, which is in good agreement with the measured spectra. In Figure 6(b3) both sets of peaks begin to overlap, and the positions of the two envelopes become less obvious. As one moves toward even shorter periods the two envelopes can no longer be resolved, as their widths become much larger than their spacing. As a consequence of these shorter periods the number of observable satellite peaks decreases. Figure 6(b6), which represents the diffraction spectrum of a superlattice with $P = 2$ nm, shows only the zero-order superlattice peak which is located approximately midway between the expected peaks for pure AlN and pure GaN. The peak corresponds to an interplanar spacing of 0.252 nm, which is intermediate between the spacings of the (0002) planes of AlN (0.249 nm) and GaN (0.258 nm) and represents the average spacing of the (0002) planes in the superlattice. Satellite peaks for this sample are out of the range of the scan, and are expected to be at $\approx 28^\circ$ and $\approx 36^\circ$. As noted below, TEM results show a well defined layered structure; thus, there is no reason to believe that this peak arises from the homogeneous mixing of the two materials.

For superlattices with periodicities over 20 nm (see Figures 6(b1–b2)) the center of GaN envelope coincides with the GaN buffer layer peak. This indicates that both have the same vertical lattice spacings. Since the center of the AlN envelope also appears at the same angular position as one would expect for the (0002) peak of pure AlN, this indicates that individual layers at periods larger than 20 nm have unchanged vertical lattice parameters and thus are relaxed with respect to each other. At periods smaller than 20 nm the positions of the envelopes start changing (compare Figures 6(b2–b3)). This is believed to be related to the lattice distortion due to elastic strain. However, since the overlapping of both envelopes starts at about the same layer period, the quantitative displacements of the centers are not clear, and become

even less evident at superlattices with periods smaller than 10 nm (see Figures 6(b4-b6)). In order to more accurately determine the transition between relaxed and strained structures, the reflections from the planes with mixed indices (for example $(10\bar{1}1)$) should be studied.

Transmission Electron Microscopy. Transmission electron microscopy (TEM) (Hitachi H-800) and high resolution microscopy (HREM) (JEOL 200CX) were used to further analyze the AlN/GaN layered structures. Cross-sectional TEM specimens were prepared using standard techniques[26].

The periodicities calculated from the x-ray spectra were confirmed by the TEM images. Discrepancies between the two methods were found to be less than 5%.

Superlattices grown on α -SiC showed a high degree of crystallinity, which has been confirmed by RHEED, X-ray diffraction, and transmission electron diffraction. Figure 7 shows a TEM image of 5 nm thick layers of AlN and GaN. GaN layers are dark; those of AlN are light. Layers are well defined and have few structural defects.

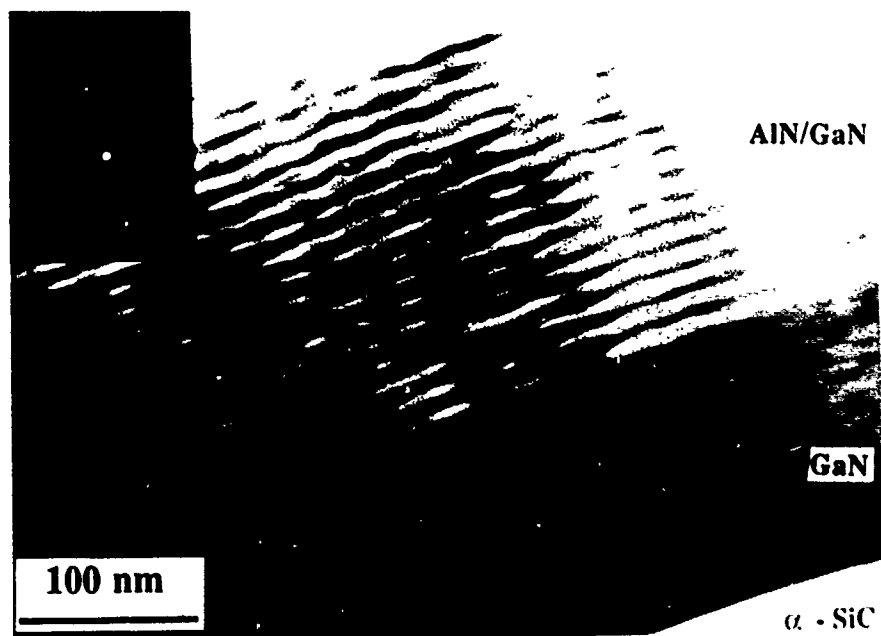


Figure 7. AlN/GaN layered structure grown on $\alpha(6H)$ -SiC. The thickness of the individual layers is 5 nm.

The (10 $\bar{1}$ 1) diffraction pattern (inset), taken from the layered structure, confirms the monocrystalline nature of the film with a low density of structural defects. The slight waviness of the layers appears to start at the buffer layer; it becomes more defined toward the top of the film. Similar phenomenon has been observed in GaAs/GaAlAs systems[29, 30] and is induced due to the optimum growth temperature difference between the two materials. In the films with thicker AlN/GaN layers this effect is observed as interface roughness between the individual layers, rather than waviness of the layers. This can be seen in Figure 8 which shows 20 nm thick layers.



Figure 8. AlN/GaN layered structure grown on α (6H)-SiC. The thickness of the individual layers is 20 nm.

By contrast, structures grown on sapphire were oriented polycrystalline. These films showed a columnar structure. The range of misorientation of the individual crystallites, measured from the lattice fringes, was found to be from 0° to 8° . However, layers of the two materials within individual crystallites are well defined and no misfit dislocations or other defects have been found. The HREM image of 3 nm thick individual layers in Figure 9 indicates perfectly strained material, with uninterrupted lattice fringes at the transitions from one material to the other. Even the structure containing 0.5 nm thick AlN layers (2 monolayers) and 1 nm thick AlN layers (4 monolayers), shown in Figure 10, shows very good compositional contrast between the individual layers.

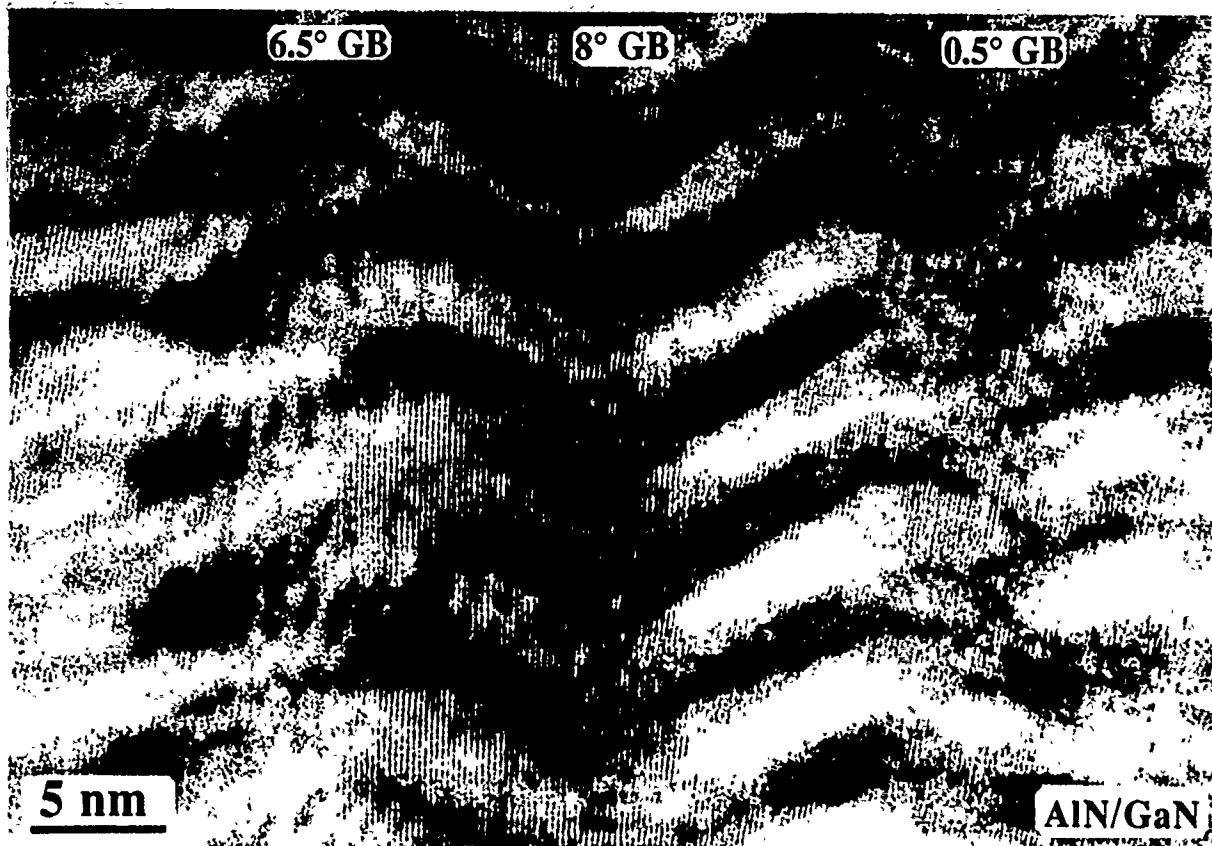


Figure 9: AlN/GaN layered structure grown on sapphire. The thickness of the individual layers is 3 nm. Note misorientation of the individual crystallites in the columnar structure.

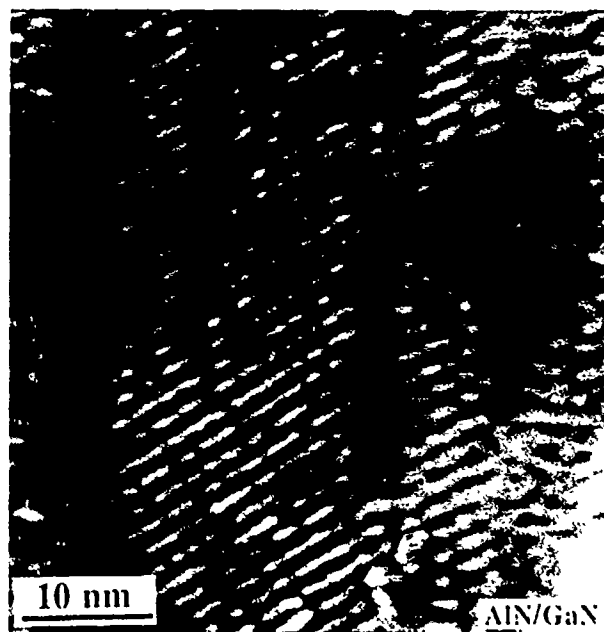


Figure 10: AlN/GaN layered structure grown on sapphire. The thickness of AlN and GaN layers is 0.5 nm and 1 nm, respectively.

E. Optical Characterization

The samples grown on $\alpha(6H)$ -SiC were characterized optically by cathodoluminescence. The spectra were taken at 77 K in the wavelength range of 200 to 800 nm using the excitation electron beam energies of 7 keV.

The bandgap difference between AlN and GaN is almost 3 eV. Thus layers of these two materials produce almost one order of magnitude larger band discontinuities than are achieved in AlGaAs or InGaAs systems. As such, AlN/GaN superlattices may provide some interesting insights regarding the behavior of electrons and holes. For example, they have potential of providing several well-separated confined electronic states.

Spectra taken from the samples with AlN/GaN layer thicknesses of 1/1, 0.5/1, 3/3, and 10 nm/10 nm (0.25 nm \approx one monolayer) are shown in Figure 11. Each spectrum consists of a broad structure centered around \approx 500 nm (2.5 eV), and a well defined peak at a higher energy. The former is due to the luminescence from the α (6H)-SiC substrate.

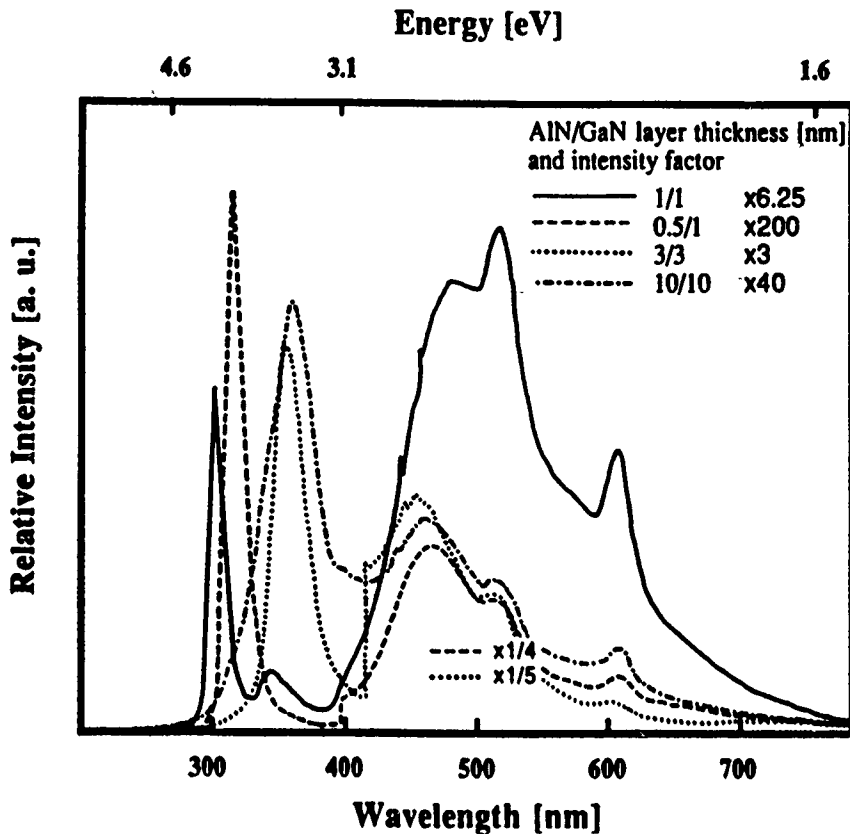


Figure 11: Cathodoluminescent spectra taken at 77K of the AlN/GaN layered structures with different periodicities. Broad peak above 400 nm is due to SiC substrate. High energy peaks are from AlN/GaN layers. Emission energy decreases with increasing GaN well thickness (1/1, 3/3, 10/10) and decreasing AlN barrier thickness (1/1, 0.5/1)

The higher energy peak increases in energy as the thickness of the layers in different samples decreases. The peak position moves from 3.42 eV for the sample with 10 nm thick wells and barriers, to 4.11 eV for the sample with 1 nm layers. The emission energy from a multi-quantum well structure is expected to also decrease if the well thickness remains constant and the barrier thickness decreases. This effect,

which is due to an increase in tunneling probability through thinner barriers, is demonstrated in peaks 1/1 and 0.5/1 which are from structures with 1 nm thick GaN wells and 1 nm and 0.5 nm thick AlN barriers, respectively.

Peaks at higher energies are also expected for AlGaN solid solutions. For example, the emission at 4.1 eV is expected for a molar concentration of Al of 0.32[19]. According to the structural and chemical analyses, there is no reason to believe that a homogeneous solid solution close to this composition had formed. Moreover, random mixing, which may be to some extent present at rough interfaces, would not result in strong, well defined peaks. On this basis, we interpret the high energy peak to be due to the recombination of the electrons and holes confined in the GaN wells. As such, we believe, that the spectra demonstrate the formation of the quantized electronic states.

A computer model for the calculation of the band structure of AlN/GaN superlattices has been developed and a comparison between the theory and experiments has been made. Two different cases were examined: 1) The emission energy shift as a function of the layer thickness, while the thicknesses of GaN and AlN layers were maintained equal (i. e. $t_{\text{AlN}} = t_{\text{GaN}} = \frac{P}{2}$), and 2) emission energy shift as a function of the barrier thickness (AlN), while the well thickness (GaN) was maintained constant at 1 nm.

The allowed energy bands for the electrons in the conduction band and for the holes in the valence band in the superlattice were calculated using a one-dimensional Krönig-Penney model[31]. According to this an electron or a hole can occupy a particular energy state in the superlattice only, if the following is true:

$$\left| \cos \left[\frac{t_1(2mE)^{\frac{1}{2}}}{\hbar} \right] \cosh \left[\frac{t_2(2m(V-E))^{\frac{1}{2}}}{\hbar} \right] + \left(\frac{V}{E} - 1 \right)^{\frac{1}{2}} \left(\frac{V}{2E} - 1 \right) \sin \left[\frac{t_1(2mE)^{\frac{1}{2}}}{\hbar} \right] \sinh \left[\frac{t_2(2m(V-E))^{\frac{1}{2}}}{\hbar} \right] \right| \leq 1$$

E is the energy of electrons (holes), V the barrier height (band discontinuity), m the effective mass of the carriers, \hbar the Planck's constant divided by 2π , and t_1 and t_2 are the respective well and barrier widths. Since there is no "hard" value for the effective mass of electrons or holes in AlN and GaN, the average values of the available data were taken[28]. The effective mass of electrons was taken as $0.2m_0$ and that of holes as $0.8m_0$. A conduction and valence band discontinuity was chosen by variation to provide the best fit to the transition energies observed by cathodoluminescence. The best fit was obtained when one half of the total bandgap discontinuity (1.4 eV) was assigned to the conduction band and one half to the valence band. The total bandgap discontinuity was calculated as the difference between the bandgaps of AlN and GaN. For the lack of data on the mechanical properties of semiconducting nitrides, the effect of the biaxial strain on the bandgap shift could not be included in the calculation, although it is expected to have a considerable influence on the bandgap of both materials.

The shaded areas in Figure 12(a) represent the lowest four calculated energy bands for the electrons in the conduction band and the holes in the valence band as a function of the individual layer thickness while the thicknesses of the AlN and GaN were kept equal. The lowest transition energy in the superlattice at a particular layer thickness is obtained as the distance between the lower edge of the first energy band for the electrons and the upper edge of the first energy band for the holes. The arrows indicate the transitions in the structures with 1, 3, and 10 nm thick AlN and GaN layers. The length of the arrows corresponds to the emission energy observed by the cathodoluminescence. The luminescence spectra for mentioned three structures are shown in Figure 12(b). The spectra show sharp and well defined peaks with the energies above the bandgap of GaN. The width of the peaks increases with the layer thickness as the superlattice makes a transition from the pseudomorphic to a relaxed structure. The measured and calculated transition energies for these superlattices are collected in Table IV.

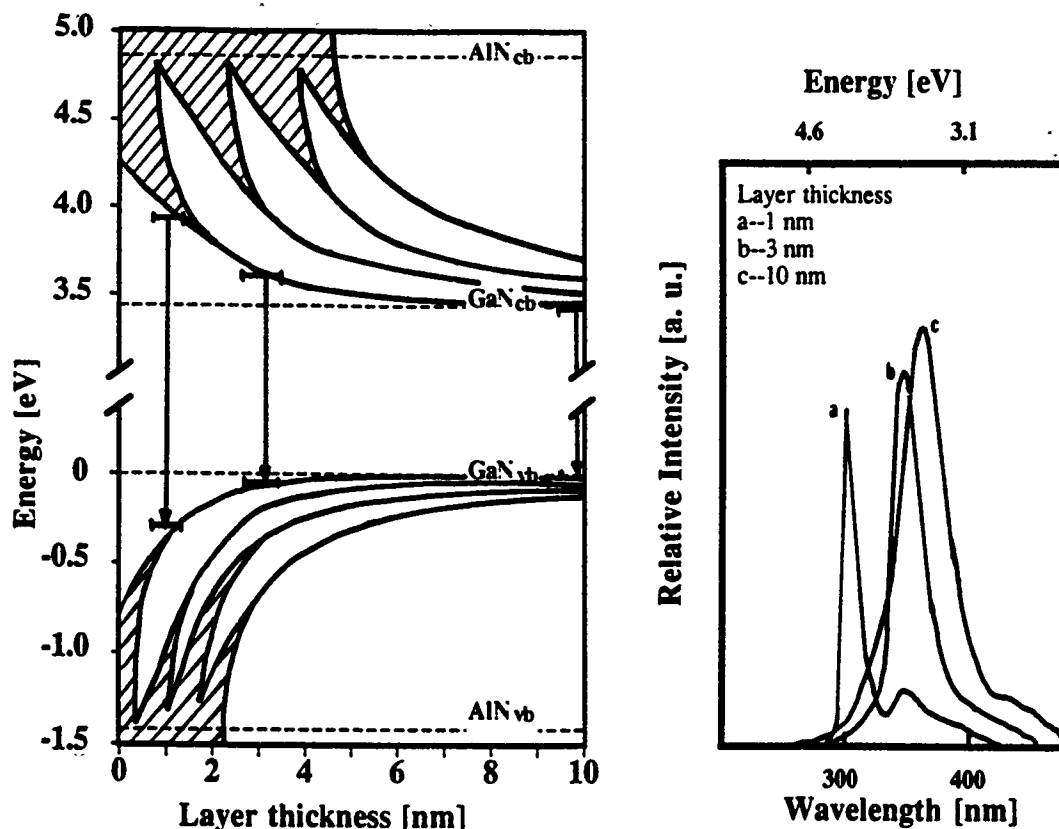


Figure 12: (a) The lowest four calculated energy bands for the electrons in the conduction band and the holes in the valence band as a function of the individual layer thickness while the thicknesses of the AlN and GaN were kept equal. The arrows indicate the transitions in the structures with 1, 3, and 10 nm thick layers, whose cathodoluminescence spectra shown in Fig. 12(b).

TABLE IV. Calculated and measured transition energies for different layer thicknesses.

Layer thickness [nm]	$E_{\text{calculated}}$ [eV]	E_{measured} [eV]	ΔE [meV]
1	4.29	4.11	180
3	3.64	3.47	170
10	3.42	3.42	≈ 0

Similar to the Figure 12(a), show the shaded areas in Figure 13(a) the lowest two energy bands for the electrons and the lowest three energy bands for holes as a

function of the barrier width at a constant well width of 1 nm. The arrows again indicate the measured transition energy of a particular structure. The measured luminescence spectra for 0.5 nm and 1 nm thick barriers are shown in Figure 13(b). The calculated and measured energies are summarized in Table V.

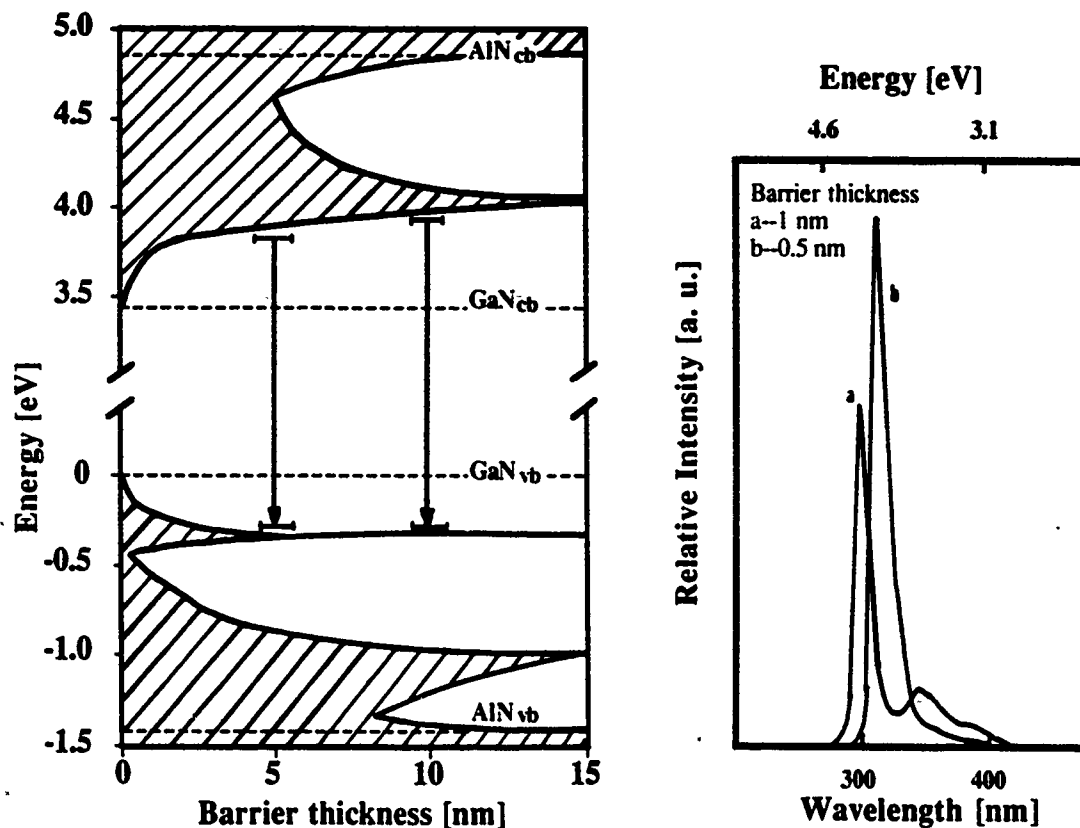


Figure 13: (a) The lowest two energy bands for the electrons and the lowest three energy bands for the holes as a function of the barrier width at a constant well width of 1 nm. The arrows indicate the measured transition energy of a particular structure. The measured luminescence spectra for 0.5 nm and 1 nm thick barriers are shown in Fig. 13(b).

A quick examination of both tables tells us the following facts: 1) The highest transition energy shift observed in this study was above 700 meV and occurred for the superlattice with 1 nm thick barriers and wells. 2) The emission energy shift for the superlattice with 0.5 nm thick barriers was slightly lower than the value above due to better coupling between adjacent wells (higher tunneling probability due to thinner

TABLE V. Calculated and measured transition energies for different barrier thicknesses.

Layer thickness [nm]	$E_{\text{calculated}}$ [eV]	E_{measured} [eV]	ΔE [meV]
0.5	4.19	3.93	260
1.0	4.29	4.11	180

barriers). 3) There exists an energy offset between the calculated and measured values, which was in the range of experimental error for 10 nm thick layers and increased to 170 meV for thinner layers and even up to 260 meV for superlattices with the thinnest barriers.

The reasons for the observed offset can be several. 1) There exists a possibility that the values for the effective masses used in the calculation are not accurate. For example if the effective masses were larger, one would obtain lower theoretical value for the transition energies and as such also lower offset. 2) The lattice mismatch between AlN and GaN produces strain, which induces bandgap shift in both materials. This shift is expected to be rather high for the materials with 2% misfit (i. e. in the range of ≈ 100 meV)[29]. 3) Interfacial mixing of Al in GaN and Ga in AlN in the monolayer scale could significantly change the transition energy in superlattices having individual layers only a few monolayers thick.

The offset for the moderately thin layers (1 and 3 nm) seems to be fairly constant (180 and 170 meV), which would not be the case if solely an error in the effective masses were in question. The fact, that the offset is negligible for thick layers (layers above the critical thickness, which are relaxed with respect to each other) and almost constant for the layers below the critical thickness (which are biaxially strained) implies the connection between the strain induced bandgap shift and the

observed offset. As such luminescence data could be a rough measure whether a layered structure is pseudomorphic or not.

The offset for the superlattices with two monolayer thick barriers is even larger than that of superlattices with moderately thin individual layers for additional 90 meV. This jump, which could not be induced by the strain is most likely the consequence of interfacial mixing, which lowers the barrier height and as such decreases the transition energy. A more sophisticated model, which would include bandgap shift due to elastic strain and also assume one monolayer of interfacial mixing is expected to give much better agreement between the experiment and theory.

IV. Design and Construction of a Gas-Source MBE/ALE System for the Deposition of AlN/GaN/SiC Pseudomorphic Heterostructures

A. Introduction

A system for the growth of AlN/GaN/SiC pseudomorphic heterostructures by the techniques of gas-source molecular beam and atomic layer epitaxy has been designed, and the various parts purchased. The assembly is currently nearing completion. This deposition system will be used initially for low temperature growth of individual monocrystalline thin films of SiC and AlN followed by SiC/AlN solid solutions and SiC/AlN/GaN pseudomorphic structures of which some or all of the layers will be solid solutions. The techniques of molecular beam and atomic layer epitaxy (MBE) (ALE) allows for precise control of growth parameters and minimization of sample contamination. The mean free path of source atoms or molecules at pressures used in MBE and ALE is much longer than the dimensions of the growth chamber. Intermolecular collisions within the growth chamber are unlikely. Parameters such as growth thickness can thus be controlled and reproducibly obtained using this technique. Gaseous species will be provided to the sample surface using a pressure-controlled flow system.

B. Growth System and Concepts of Gas Flow Control

A schematic of the system to be used for gas-source MBE/ALE is shown in Figure 14. Samples are introduced into a small load lock chamber which is then evacuated. The samples are subsequently transferred to the heating stage in the growth chamber. The load lock is used in order to increase sample throughput, as well as to keep the main deposition chamber under vacuum while samples are exchanged. It is pumped by a Balzers TPU 060 turbomolecular pump backed by a Sargent-Welch rotary vane pump. The load lock is operational, and pressures of 1×10^{-6} torr or below are easily reached in 30 minutes.

The growth chamber will be used for both *in situ* sample cleaning and deposition. Substrates will be cleaned prior to deposition by using an Ar^+ plasma to produce H^+ radicals from H_2 introduced into the system downstream from the plasma. The Ar^+ plasma will be obtained using an electron cyclotron resonance (ECR) plasma source developed in our laboratory (25). This source is currently under construction in our machine shop. To date, no published work has been performed on plasma cleaning of $\alpha\text{-SiC}$. H^+ plasma cleaning of Si using this method has been achieved at 300°C [32].

Samples will be heated using a coiled tungsten filament contained within a SiC-coated graphite cylindrical heating cavity lined with molybdenum and tungsten shielding. A high-purity pyrolitic BN disk will be used as an insulating plate for holding the W coil. The heater will be capable of temperatures of over 1000°C . Samples will be rotated during growth.

Species used in growth are introduced by way of the source flange. The source flange is equipped with ports for up to five solid sources and five gaseous sources. Disilane (Si_2H_6) will be used as a source of silicon, and will be supplied through a pressure-controlled flow system described in the next section. Ethylene (C_2H_4) will be used as a source of carbon. It will be introduced through a specially designed ECR

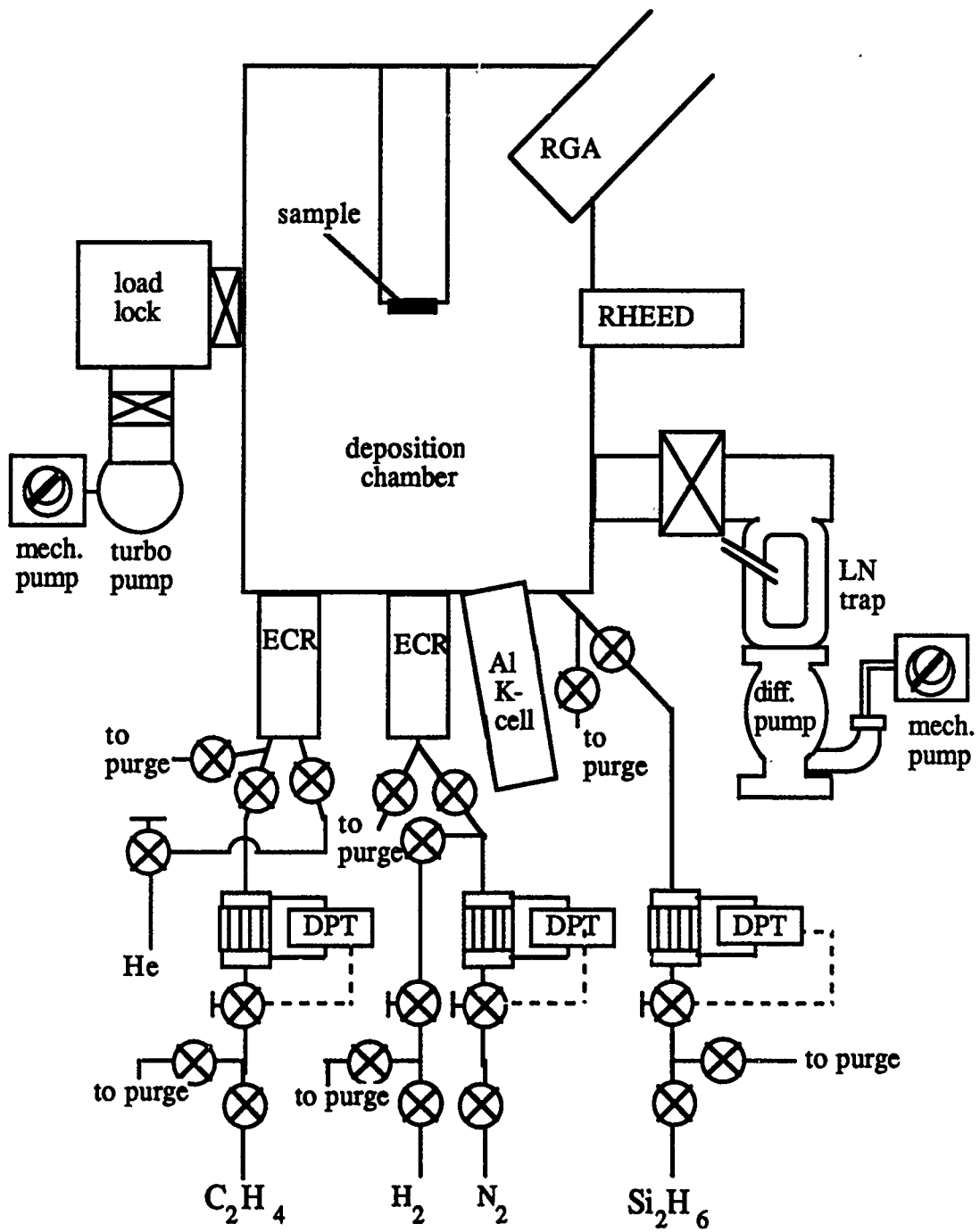


Figure 14: Schematic of Molecular Beam Epitaxy System

plasma source. This source will enable the introduction of ethylene downstream of an induced Ar^+ plasma. Aluminum will be evaporated from a solid-source MBE effusion cell made by EPI Systems while gallium will be derived from the decomposition of triethylgallium. Diatomic nitrogen (N_2), decomposed with an ECR plasma will be used as a source of atomic and imized of nitrogen. Mechanical air-actuated shutters will be used with all sources to enable rapid switching between sources.

In the case of gas-source MBE and ALE, the distance between collisions for each molecule is much longer than the dimensions of the deposition chamber. This implies that flow is in the molecular regime, and flow rates are too low for standard mass flow controllers. A method of flow measurement and control has been developed which works well in the molecular regime[33]. It is based on the fact that in molecular flow, the conductance of a cylindrical tube is not a function of pressure. The mass flow, Q , through an element can be expressed as

$$Q = C\Delta P$$

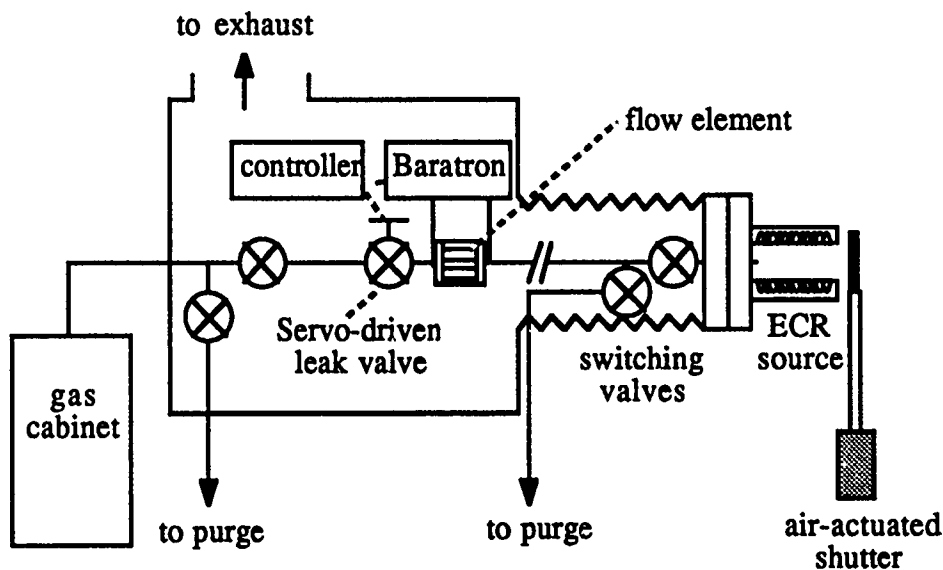


Figure 15: Valving System for Gaseous Sources

where ΔP is the pressure difference and C is the conductance. The conductance of a cylindrical tube or series of cylindrical tubes in molecular flow can be accurately

calculated. If the pressure difference across this element of known conductance is measured, then the flow rate through this element can be easily found. The equipment used consists of a MKS CFE-0.5 precision molecular flow element, a MKS Model 120 differential capacitance manometer to measure the pressure difference across the element, and a Granville-Phillips Model 216 servo-driven leak valve and controller to control the gas flow to the element. The gas flow control system configuration is shown in Figure 15. Each gas used has its own flow control system. The entire flow control system, from the gas cabinet to the deposition chamber, will be exhausted for safety considerations. This type of system has been shown to enable the precise control of gas flow in the molecular regime, and can switch gases on in about 1 second and off in about 2 to 4 seconds[34].

The chamber also contains a UTI-100C mass spectrometer, which will be used in order to determine species present during growth. Characterization of films using RHEED during growth is also planned. The system is pumped using a Varian VHS-6 2400 l/s diffusion pump with a Vacuum Generators UHV liquid nitrogen cold trap backed by a rotary vane pump. Background pressures in the 10^{-10} torr range are obtainable in this system.

C. Discussion

Low temperature growth of high-purity, pseudomorphic, monocrystalline layers of AlN, GaN and SiC and solid solutions of these compounds on β - and α -SiC substrates is the primary goal of this project. These SiC films will be grown on β -substrates grown in-house and α -SiC substrates obtained from Cree Research described elsewhere in this report. The primary obstacle to low-temperature growth of SiC is the difficulty in locating a suitable source for monomolecular carbon. Several methods for the deposition of solid carbon have been considered. The most promising of these is resistive heating of a graphite filament [35]. If the filament is heated to around 2500°C, a significant flux of carbon leaves the sample due to thermal

evaporation. The majority of C leaving the filament has been shown to be monomolecular in nature. This method has been utilized for carbon doping of GaAs in an MBE system. Huge amounts of power and a filament with very large cross-section would be necessary in order to obtain a flux sufficient for MBE growth of a binary carbide such as SiC. This fact precludes the use of this method at this time in this project. Other potential methods for solid-source deposition of C, such as laser evaporation and electron-beam evaporation, do not as yet yield large percentages of monomolecular carbon.

Gaseous sources of carbon such as hydrocarbons are relatively difficult to decompose. The growth temperature of SiC can be substantially lowered if the energy required for this decomposition can be decreased. One method which is useful in some instances is laser decomposition. High-energy monochromatic light, such as that produced by a laser, can impart sufficient energy to gaseous molecules to decompose them. Laser-enhanced chemical vapor deposition is a well-known technique for obtaining lower-temperature growth of many materials at pressures near one atmosphere. However, the efficiency of the decomposition process in the pressure range used in this research is extremely low.

Plasma decomposition is a proven method for low-temperature decomposition of gaseous species. The feasibility of an ECR source for monocrystalline growth of various materials in an MBE environment has been demonstrated[36,37]. Decomposition of ethylene will utilize a previously mentioned NCSU-developed ECR source modified to allow the downstream introduction of a gaseous species. Downstream introduction of a carbon-containing species is necessary because of the electrically conducting nature of carbon deposits on the inside of the microwave cavity. Argon gas will be used to sustain the plasma. Valving will be placed as close to the source as possible to minimize dead space and enable the rapid switching on and off of the ethylene supply.

In addition to SiC films, SiC/AlN pseudomorphic layers and solid solutions will also be grown as a part of this research. Al and N will also be used as the primary dopants in SiC. Suitable sources of Al and N are thus required for this research. Nitrogen will be obtained by ECR plasma decomposition of N₂. MBE deposition of Al is possible either by thermal decomposition of an organometallic source, or thermal evaporation of solid Al using an effusion cell. Both types of sources are commonly used in molecular beam epitaxy. However, thermal decomposition of triethylaluminum (TEAl) and trimethylaluminum (TMAI) at temperatures above 600°C has long been known to result in significant carbon concentrations in GaAs films[38]. A relatively unknown organometallic source, triisobutyl-aluminum (TIBAl) has been shown to result in much lower carbon concentrations in Al films relative to other alkyls[39]. However, carbon concentrations on the order of 0.1 percent in GaAs grown by gas-source MBE still result from temperatures in the 700°C range using TIBAl. This is undoubtedly too high for electrical applications of AlN. As a result, a solid-source effusion cell will be used for Al deposition.

Once all components are received and are in place, growth experiments will begin. Initially, the characterization of the plasmas obtained from both the C and N ECR sources will be performed. Conditions will be optimized for plasma formation on both sources. Initial experiments will be run to determine optimum growth conditions for gas-source MBE of monocrystalline SiC and AlN on α -SiC. These will consist of varying substrate temperature and flow rates of Si, C and N source gases and temperature of the Al effusion cell for growth on both the (0001) Si face and (0001) C face of 6H-SiC. Characterization of these films using electron and optical microscopy as well as electrical measurements will be performed. In addition, chemical analysis using Scanning Auger Spectrometry and secondary ion mass spectrometry (SIMS) will be performed to determine the stoichiometry of the major elements and the concentrations of any trace impurities. Planned experiments also include eventual n-

and p-type doping of SiC, growth of GaN, and growth of AlN/SiC and AlN/GaN solid solutions and pseudomorphic layers.

D. Conclusions

A system for growth of monocrystalline AlN, GaN and SiC thin films and SiC/AlN and GaN/AlN solid solutions and pseudomorphic structures using gas-source MBE and ALE has been designed and is nearing completion. This system consists of a loading chamber and a deposition/cleaning chamber. Samples will be cleaned prior to deposition using H^+ introduced downstream of an Ar^+ electron cyclotron resonance-induced plasma. The deposition chamber has the capability of using both solid and gaseous sources, and both will be used in this research. Gas flow will be controlled using a flow system based on measurement of the pressure drop across an element of constant conductance.

Gaseous sources will be used for silicon, carbon, gallium and nitrogen. Silicon will be deposited by thermal decomposition of disilane. Ethylene will be decomposed to an activated carbon-containing species using an electron cyclotron resonance plasma. Triethylgallium will be used as the source of Ga. And molecular nitrogen will be decomposed using an ECR plasma. An MBE effusion cell will be used as a solid source for aluminum. Initial growth experiments will commence in the near future, as well as characterization of films grown by this process.

V. References

1. S. Koizumi, T. Murakami, T. Inuzuka, K. Suzuki, "Epitaxial Growth of diamond thin films on cubic boron nitride {111} surfaces by DC plasma chemical vapour deposition." Submitted to Appl Phys Lett. (May 30 1990).
2. M. Yoshikawa, H. Ishida, A. Ishitani, T. Murakami, S. Koizumi, T. Inuzuka, "Study of crystallographic orientations in the diamond film on c-BN using Raman Microprobe," Submitted to Appl Phys Lett. (May 30 1990).
3. N. H. Fletcher and K. W. Lodge, "Epitaxial Growth, Part B," J. W. Matthews ed, Academic Press, New York, (1975) 529.

4. M. W. H. Braun, "Epitaxy on substrates with hexagonal lattice symmetry" DSc Thesis, University of Pretoria Nov 1987.
5. M. W. H. Braun, J. H. van der Merwe, South African J. of Science **84**, 670 (1988).
6. J. H. van der Merwe and Phil Mag **45**, 127, 145, 159 (1982).
7. H. Reiss, J Appl Phys **39**, 5045 (1968).
8. F. C. Frank and J. H. van der Merwe, Proc Roy Soc A **198**, 205, 216 (1949); A **200**, 125, 261 (1950).
9. J. H. van der Merwe, Proc Phys Soc, (London) A **63**, 616, 1370 (1950).
10. Y. Gotoh and I. Arai, Japan J Appl Phys **25**, L583 (1986).
11. G. Busch and H. Schade, "Lectures on Solid State Physics," Ferdinand Cap transl, Pergamon Press, Oxford, 16 (1976).
12. C. Kittel, "Introduction to Solid State Physics," John Wiley and Sons, New York, 4 ed, (1971), p. 43.
13. L. A. Bruce, H. Jaeger and Phil Mag **36**, 1331 (1977); **37**, 337 (1978); **38**, 223 (1978).
14. P. M. Stoop and J. A. Snyman, Thin Solid Films **163**, 503 (1989).
15. M. A. van Hove and K. Hermann, LATUSE and SARCH, Univ of California, Berkeley, Ca 94720, USA.
16. Landolt-Börnstein Tables, "Numerical Data and Functional Relationships in Science and Technology," New Series **III/17d**, "Technology of III-V, II-VI and Non-Tetrahedrally Bonded Compounds," Springer Verlag, Berlin.
17. R. F. Davis, Z. Sitar, B. E. Williams, H. S. Kong, H. J. Kim, J. W. Palmour, J. A. Edmond, J. Ryu, J. T. Glass, and C. H. Carter, Jr., Mat. Sci. & Eng. **B1**, 77 (1988).
18. P. M. Dryburgh, J. Cr. Growth **94**, 23 (1989).
19. Y. Koide, H. Itoh, M. R. H. Khan, K. Hiramatu, N. Sawaki, and I. Akasaki, J. Appl. Phys. **61**, 4540 (1987).
20. W. T. Tsang, Appl. Phys. Lett. **39**, 786 (1981).
21. M. G. Burt, Electron. Lett. **19**, 210 (1983).
22. P. Davson, G. Duggan, H. I. Ralph, and K. Woodbridge, Superlattices and Microstr. **1**, 173 (1985).

23. N. Holonyak, Jr., R. M. Kolbas, R. D. Dupuis, and P. D. Dapkus, *IEEE J. Quantum Electron.* **QE16**, 170 (1980).
24. M. J. Paisley, Z. Sitar, J. B. Posthill, and R. F. Davis, *J. Vac. Sci. Technol. A* **7**, 701 (1989).
25. Z. Sitar, M. J. Paisley, D. K. Smith, and R. F. Davis, submitted to *Rev. Sci. Instr.*
26. J. C. Bravman and R. Sinclair, *J. Electron Microsc. Tech.* **1**, 53 (1987).
27. M. Quillec, L. Goldstein, G. Le Roux, J. Burgeat, and J. Primot, *J. Appl. Phys.* **55**, 2904 (1984).
28. B. L. Jiang, F. Shimura, and G. A. Rozgonyi, *Appl. Phys. Lett.* **52**, 1258 (1988).
29. C. Delamarre, A. Dubon, J. Y. Laval, B. Guenais, and J. Y. Emery, *Semiconductor Quantum Well Structures and Superlattices*, *Mat. Res. Soc. Europe Proc. VI*, edited by K. Ploog and N. T. Linh, Strasbourg, France, 105 (1985).
30. D. A. Andrews, R. Heckingbottom, and G. J. Davies, *Semiconductor Quantum Well Structures and Superlattices*, *Mat. Res. Soc. Europe Proc. VI*, edited by K. Ploog and N. T. Linh, Strasbourg, France, 85 (1985).
31. For example; R. L. Liboff, *Introductory Quantum Mechanics*, Holden-Day, Inc., San Francisco (1980).
32. R. Rudder, G. Fountain, and R. Markunas, *J. Appl. Phys.* **60**, 3519 (1986).
33. R. A. Kiesling, J. J. Sullivan, and D. J. Santeler, *J. Vac. Sci. Technol.* **15**, 771 (1978).
34. H. Ishikawa, H. Ando, K. Kondo, A. Sandhu, E. Miyauchi, T. Fujii, and S. Hiyamizu, *J. Vac. Sci. Technol. A* **8**, 805 (1990).
35. R. J. Malik, R. N. Nottenberg, E. F. Schubert, J. F. Walker, and R. W. Ryan, *Appl. Phys. Lett.* **53**, 2661 (1988).
36. Z. Sitar, M. J. Paisley, B. Yan, J. Ruan, W. J. Choyke, and R. F. Davis, *J. Vac. Sci. Technol. B* **8**, 316 (1990).
37. N. Yamamoto, N. Kondo, and Y. Nanishi, *J. Cryst. Growth* **96**, 705 (1989).
38. M. Weyers, N. Pütz, H. Heinecke, M. Heyen, H. Luth, and P. Balk, *J. Electron. Mater.* **15**, 57 (1986).
39. B. J. Lee, Y. M. Houg, and J. N. Miller, to be published in *J. Cryst. Growth*.